

Adaptive Multi-Fidelity Structural Optimization under Fluid-Structure Interaction

Aditya Narkhede^{a,b}, Erick Rivas^a, Kevin Wang^{a,*}

^aKevin T. Crofton Department of Aerospace and Ocean Engineering, Virginia Tech, Blacksburg, VA, USA

^bDepartment of Mechanical Engineering, University of British Columbia, Vancouver, BC, Canada

Abstract

The design of structures and vehicles subject to fluid-structure interaction (FSI) often requires high-fidelity coupled analysis. While the design variables pertain to the structure, the computational cost is usually dominated by the fluid solver, making iterative optimization prohibitively expensive. This paper presents an adaptive multi-fidelity optimization method that combines high-fidelity FSI analysis with a lightweight surrogate for fluid-induced loads and a decision model that selects between surrogate and high-fidelity fluid evaluations. During optimization, results from completed FSI analyses are used to incrementally update a non-intrusive surrogate model based on nearest-neighbor search and radial interpolation. To maintain accuracy across varying geometries, a hybrid Lagrangian-Eulerian mapping function is developed to transfer fluid loads between structural designs. The evolution in surface orientation is handled through decomposition of the traction vectors in local orthonormal bases. An adaptive Gaussian process regression model is employed to predict surrogate error and quantify uncertainty, allowing risk-aware selection of when coupled analysis is required. As design evaluations cluster near the optimal solution, the accuracy of the surrogate model naturally improves, thereby reducing the reliance on high-fidelity fluid evaluations. This optimization framework treats the high-fidelity FSI model as the ground truth, instead of a pre-computed dataset. It requires no offline training, preserves the high-fidelity structural model in all design evaluations, and ensures that the final design is evaluated by high-fidelity FSI analysis. The fundamental idea is justified theoretically using a simplified model problem, which shows that the leading-order error is a monotonically increasing, concave, and bounded function of the fluid added mass. The framework is implemented using open-source software and demonstrated numerically through two benchmark examples. For shape optimization of a flexible panel under shock loading, results show an 80% reduction in computational cost while maintaining accuracy within 2.3% of fully high-fidelity FSI optimization.

Keywords: fluid-structure interaction, structural optimization, multi-fidelity analysis, Gaussian process regression, surrogate model,

*Corresponding author.

Email address: kevinw3@vt.edu (Kevin Wang)

1. Introduction

The motion and deformation of structures in fluid environments are inherently coupled with the fluid flow. When a structure is lightweight and flexible, or the fluid has a high density (e.g., liquids), fluid-structure interaction (FSI) can significantly alter the structure’s performance and integrity compared to how it would behave in vacuum or a steady flow. The design of structures subject to FSI is often motivated by the pursuit of energy efficiency [1, 2], maneuverability [3, 4], and biomimicry [5, 6]. Another class of applications involves systems specifically designed to withstand mechanical or thermal loads transmitted through a fluid medium, such as shock-absorbing armor and explosion containment chambers [7, 8].

In such cases, predicting structural dynamics requires coupling it with the surrounding fluid dynamics, although the fluid itself may not be the primary concern. Over the past few decades, a major development in computational mechanics has been the integration of computational fluid dynamics (CFD) and computational structural dynamics (CSD) for high-fidelity FSI analysis. Research efforts have been made to reconcile the different (Eulerian and Lagrangian) reference frames used to formulate fluid and structural kinematics [9, 10], to enforce interface conditions on moving boundaries [11, 12], and to maintain numerical stability and accuracy [13, 14]. This body of work has also intersected with research on conjugate heat transfer, allowing both mechanical and thermal exchanges across the material interface [15, 16, 17].

In this paper, we consider the numerical optimization of structures subject to FSI. The governing partial differential equations (PDEs) of the fluid and structure naturally appear as equality constraints. While coupled CFD–CSD analyses can be used to evaluate these constraints, their computational cost is often prohibitive for the iterative optimization process. To reduce the cost, a conceptually straightforward idea is to treat the coupled analysis as a black box, and approximate its input-output relation using statistical models. This approach, known as surrogate-based analysis and optimization (SBAO) [18, 19], is non-intrusive in that it does not require modification of the CFD and CSD solvers. However, it is not specifically tailored to FSI problems, and does not distinguish the fluid and structural responses [20, 21, 22].

In coupled CFD–CSD analyses, the computational cost of the fluid solver is often far greater than that of the structure. As fluids do not resist shape changes, the region of fluid flow interacting with a solid structure is typically much larger than the structure itself. The widespread use of efficient geometric representations (e.g., beam and shell elements) further reduces the cost on the structural side. Meanwhile, the design variables are often associated with the structure rather than the fluid. This imbalance between computational cost (dominated by the fluid) and optimization “relevance” (dominated by the structure) motivates a strategy that may be well-suited to FSI-constrained structural optimization: retaining the high-fidelity CSD model while accelerating the fluid analysis. In this way, the trade-off lies solely in the accuracy of the fluid-induced loads, but not the structural analysis itself.

Different methods have been explored to construct computationally efficient models of fluid dynamics. One approach is to simplify the governing equations by idealizing the flow physics. Examples include potential-flow panel

methods and free-field blast wave models (e.g., the Friedlander equation), which have been integrated with structural dynamics in aeroelasticity and blast response analyses [23, 24, 25]. These models are intuitive and do not require large datasets for calibration. Reduced-order models (ROMs) represent another approach in which full-field flow solutions are sought within low-dimensional subspaces constructed from pre-computed CFD results. In most cases, the nonlinear flux functions in the governing equations also need to be approximated through linearization or “hyperreduction” to achieve the expected cost reduction [26, 27]. Some ROMs have been used in FSI analyses as substitutes for the original CFD model, leading to speedups by several orders of magnitude [28, 29]. More recently, deep neural network (DNN)-based surrogates have gained attention. Autoencoders and decoders comprised of linear operators and nonlinear scalar activation functions have been used to map between high-dimensional flow fields and low-dimensional latent spaces [30, 31, 32, 33]. In many cases, DNN surrogates are trained on CFD data, and represent input-output mappings rather than the underlying physics. Nonetheless, physical constraints can be incorporated into the loss function or enforced in the network architecture [34, 35].

All these models can be used in FSI-constrained structural optimization. However, simplified physical models are often inaccurate because the underlying assumptions are rarely satisfied in practical applications. For example, Narkhede *et al.* demonstrated that for a shock mitigation application, approximating the flow using empirical blast models can lead to 37% error in the structure’s maximum plastic strain [8]. On the other hand, data-driven approaches typically require a large number of expensive CFD analyses to generate solution bases (for ROMs) and training data (for DNNs). The accuracy of these models depends heavily on how well the CFD analyses sample the relevant parameter space (e.g., operating conditions or structural geometry) [36]. Because such models are constructed offline, prior to the optimization, the number of CFD analyses required for model generation can exceed that needed to complete the optimization directly using coupled CFD–CSD analyses. For example, in Bouhlel *et al.* [37], approximately 42,000 CFD simulations were performed to train a deep learning surrogate for airfoil shape optimization. While these models become advantageous when reused across many optimization problems, achieving such reusability may demand an even broader set of pre-computed results.

In this paper, we present an adaptive, multi-fidelity optimization framework that integrates coupled CFD–CSD analysis with two additional components:

- (1) a surrogate model of the fluid-induced loads on the structural surface, constructed and updated on-the-fly during the optimization process, and
- (2) a decision model that estimates the surrogate’s error and determines, for each design point, whether to employ the surrogate or the original CFD model.

The optimization process begins with coupled CFD–CSD analyses to evaluate the initial design candidates. As the process advances, the resulting CFD data are progressively used to build and refine the surrogate model of the fluid loads. Because the available data grow only gradually with each iteration, the surrogate model should be lightweight and adaptive rather than heavily parameterized. In this work, we employ nearest-neighbor search and unstructured

local interpolation algorithms, which allow efficient updates with minimal computational overhead. As the optimization process converges, new design evaluations are increasingly concentrated around one or more local minima. This behavior is expected to improve the surrogate model’s accuracy for subsequent evaluations.

The decision model is constructed using Gaussian process regression (GPR). For each new design evaluation, it predicts whether the surrogate model is sufficiently accurate. If so, the surrogate is used to generate the fluid loads for the CSD analysis. Otherwise, the framework automatically reverts to the coupled CFD–CSD analysis, and its result is used to update both the surrogate and the decision model. GPR is well suited for this task because it provides both an estimate of the approximation error and a measure of the predictive uncertainty. In this work, the estimated error and associated uncertainty are used jointly to assess the accuracy of the surrogate model in a risk-aware manner. Moreover, the kernel function in GPR provides a flexible means to represent high-dimensional error fields as functions of the design variables, and its parameters can be calibrated progressively, allowing the decision model to be updated as the optimization proceeds.

Compared to relying completely on coupled CFD–CSD analyses, this adaptive, multi-fidelity framework is expected to maintain accuracy while reducing computational cost. It reuses the data accumulated from expensive simulations, which would otherwise be discarded after each iteration. Compared to SBAO and data-driven fluid dynamics models, this framework requires no pre-computation or offline training, preserves the high-fidelity CSD model, and continues to utilize the high-fidelity CFD model throughout the optimization process. The cost of updating and evaluating the surrogate and decision models is negligible compared to running a CFD analysis. Therefore, even in the worst case—when all design points are evaluated using coupled CFD–CSD analysis—the computational overhead remains trivial.

This framework is related to prior research on online model adaptation and adaptive fidelity selection in optimization (e.g., [38, 39, 40, 26]). However, it is formulated here specifically for FSI problems, and the disparity between fluid and structural computational costs is exploited to balance accuracy and efficiency. While the framework is conceptually applicable to both gradient-based and gradient-free optimization methods, this paper focuses on the latter, particularly genetic algorithms. Gradient-based FSI optimization is still uncommon due to the challenges of computing derivatives across coupled CFD–CSD solvers, although some recent studies have made progress in this area (e.g., [41]).

The remainder of this paper is organized as follows. In Sec. 2, we formulate the constrained optimization problem for structures subject to FSI. We also use a simplified model to justify the proposed approach by relating its performance to the added mass effect. In Sec. 3, we present the proposed optimization framework, focusing on the surrogate model of fluid-induced loads and the GPR decision model. Section 4 describes the algorithms for implementing the framework and analyzes their computational complexity. Section 5 presents two numerical experiments that demonstrate the performance of the framework. Finally, concluding remarks are provided in Sec. 6.

2. Problem Description

2.1. Optimization of structures subject to FSI

In general, PDE constraints can be handled in two ways. One approach is to treat them explicitly as equality constraints, known as simultaneous analysis and design (SAND). The other approach, referred to as nested analysis and design (NAND), is to treat the PDE as a function that maps the design variables of the optimization problem to the state variables of the PDE. Following the NAND approach, the optimization of a solid structure subject to FSI can be written as

$$\begin{aligned} & \underset{\alpha \in \Omega_D}{\text{minimize}} && c(\mathbf{w}_S(\alpha), \alpha), \\ & \text{subject to} && \mathbf{g}(\mathbf{w}_S(\alpha), \alpha) \leq \mathbf{0}, \\ & && \mathbf{h}(\mathbf{w}_S(\alpha), \alpha) = \mathbf{0}, \end{aligned} \quad (1)$$

where \mathbf{w}_S denotes the structural state variables. α represents the design variables, such as the structure's geometric and material parameters. c is the objective function being minimized. \mathbf{g} and \mathbf{h} denote the inequality and equality constraints, other than the governing PDEs. In this work, we assume that c , \mathbf{g} , and \mathbf{h} do not depend explicitly on fluid variables.

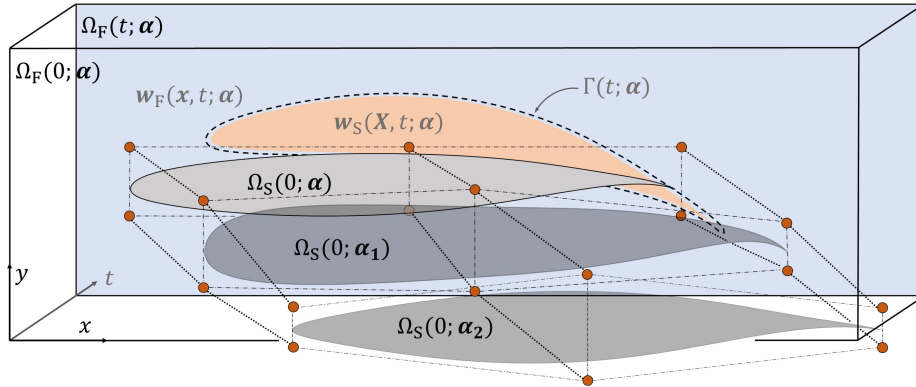


Fig. 1: Fundamental concepts in FSI-constrained structural optimization: independent variables (space \mathbf{x} , time t , and design variables α), Eulerian and Lagrangian coordinates (\mathbf{x} and \mathbf{X}), fluid and structural domains (Ω_F and Ω_S), interface (Γ), and state variables (\mathbf{w}_F and \mathbf{w}_S).

Figure 1 illustrates the problem setup. For a given design characterized by α , \mathbf{w}_S is determined implicitly by the coupled FSI problem,

$$\mathcal{R}(\mathbf{w}_F, \mathbf{w}_S; \alpha) = \mathbf{0}, \quad (2)$$

which includes the governing PDEs of fluid and structural dynamics and their initial and boundary conditions. Here, \mathbf{w}_F denotes the fluid state variables, which are obtained simultaneously with \mathbf{w}_S . This coupled problem can be decomposed into a fluid sub-problem and a structural sub-problem, i.e.,

$$\mathcal{R}(\mathbf{w}_F, \mathbf{w}_S; \alpha) := \begin{cases} \mathcal{R}_F(\mathbf{w}_F, \mathbf{w}_S) = \mathbf{0}, \\ \mathcal{R}_S(\mathbf{w}_F, \mathbf{w}_S; \alpha) = \mathbf{0}. \end{cases} \quad (3)$$

The fluid sub-problem can be written in its strong form as

$$\mathcal{R}_F : \begin{cases} \frac{\partial \mathbf{w}_F}{\partial t} = \mathcal{L}(\mathbf{w}_F) + \mathbf{s}_F(\mathbf{w}_F, \mathbf{x}, t), & \forall \mathbf{x} \in \Omega_F(t), \\ \mathcal{B}_F(\mathbf{w}_F) = \mathbf{0}, & \forall \mathbf{x} \in \partial\Omega_F(t) \setminus \Gamma(t), \\ \mathbf{w}_F(\mathbf{x}, 0) = \mathbf{w}_{F,0}(\mathbf{x}), & \forall \mathbf{x} \in \Omega_F(0), \\ \phi_1(\mathbf{w}_F, \mathbf{w}_S) = \mathbf{0}, & \forall \mathbf{x} \in \Gamma(t), \end{cases} \quad (4)$$

where $\Omega_F(t)$ denotes the time-dependent fluid domain, and $\Gamma(t)$ the fluid-structure interface that evolves due to structural motion and deformation. \mathcal{L} is the spatial differential operator in the PDE, and \mathbf{s}_F represents the source terms. For example, for a compressible inviscid flow governed by Euler equations,

$$\mathbf{w}_F = \begin{bmatrix} \rho \\ \rho \mathbf{v} \\ E_t \end{bmatrix}, \quad \mathcal{L}(\mathbf{w}_F) = -\nabla \cdot \begin{bmatrix} \rho \mathbf{v}^T \\ \rho \mathbf{v} \otimes \mathbf{v} + p \mathbb{I} \\ (E_t + p) \mathbf{v}^T \end{bmatrix}, \quad \mathbf{s}_F(\mathbf{w}_F, \mathbf{x}, t) = \mathbf{0}, \quad (5)$$

where ρ , \mathbf{v} , p , and E_t represent fluid density, velocity, pressure, and total energy per unit volume, respectively.

In (4), \mathcal{B}_F represents the boundary conditions on the boundaries other than the fluid-structure interface ($\Gamma(t)$). $\mathbf{w}_{F,0}$ is the initial condition, and ϕ_1 represents the kinematic interface condition on $\Gamma(t)$. For example, for an inviscid flow,

$$\phi_1(\mathbf{w}_F, \mathbf{w}_S) = \left(\mathbf{v} - \frac{\partial \mathbf{w}_S}{\partial t} \right) \cdot \mathbf{n}, \quad (6)$$

where \mathbf{w}_S denotes the structural displacement, and \mathbf{n} the normal direction of the interface.

The structural design variables α do not explicitly enter the fluid operator \mathcal{R}_F but influences the fluid state \mathbf{w}_F through the coupling with \mathcal{R}_S .

Unlike the fluid, the kinematics of solid structures is typically described in the Lagrangian reference frame. Let $\Omega_S(t)$ represent the structural configuration at time t . Based on the reference configuration, $\Omega_S(0)$, the structural sub-problem in (3) can be written as

$$\mathcal{R}_S : \begin{cases} \rho_S(\mathbf{X}) \frac{\partial^2 \mathbf{w}_S}{\partial t^2} = \mathcal{D}_X(J^{-1} \mathbf{F} \cdot \mathbf{S} \cdot \mathbf{F}^T) + \mathbf{s}_S(\mathbf{X}, t), & \forall \mathbf{X} \in \Omega_S(0), \\ \mathcal{B}_S(\mathbf{w}_S) = \mathbf{0}, & \forall \mathbf{X} \in \partial\Omega_S(0) \setminus \Gamma(0) \\ \mathbf{w}_S(\mathbf{X}, 0) = \mathbf{w}_{S,0}(\mathbf{X}), & \forall \mathbf{X} \in \Omega_S(0), \\ \frac{\partial \mathbf{w}_S}{\partial t}(\mathbf{X}, 0) = \mathbf{v}_0(\mathbf{X}), & \forall \mathbf{X} \in \Omega_S(0), \\ \phi_2(\mathbf{w}_F, \mathbf{w}_S) = \mathbf{0}, & \forall \mathbf{X} \in \Gamma(0), \end{cases} \quad (7)$$

where \mathbf{X} denotes the material coordinates, ρ_S is the structural density, and \mathbf{F} is the deformation gradient, with $J = \det(\mathbf{F})$. \mathbf{S} represents the second Piola-Kirchhoff stress tensor, which is related to \mathbf{w}_S through the constitutive material models. \mathcal{D}_X is the divergence operator expressed in Lagrangian coordinates. \mathcal{B}_S represents the boundary conditions on the boundaries other than the fluid-structure interface. $\mathbf{w}_{S,0}$ and \mathbf{v}_0 specify the initial displacement and velocity, respectively. The term \mathbf{s}_S represents any external source terms acting on the structure.

ϕ_2 denotes the dynamic interface condition at the fluid-structure interface. For example, for inviscid fluid flows

$$\phi_2(\mathbf{w}_F, \mathbf{w}_S) = (\boldsymbol{\sigma}_S - p\mathbb{I}) \cdot \mathbf{n}, \quad (8)$$

where $\boldsymbol{\sigma}_S$ is the Cauchy stress tensor of the structure, i.e.,

$$\boldsymbol{\sigma}_S = \frac{1}{J} \mathbf{F} \cdot \mathbf{S} \cdot \mathbf{F}^T. \quad (9)$$

The vector of design variables, $\boldsymbol{\alpha}$, may include both material and geometric properties of the structure. Therefore, ρ_S , \mathbf{S} , and $\Omega_S(0)$ may all depend on $\boldsymbol{\alpha}$.

2.2. Overview of computational approach

Although gradient-based methods are generally more efficient for continuous optimization problems, applying them to (1) is challenging. It requires computing $d\mathbf{w}_S/d\boldsymbol{\alpha}$ from the coupled system \mathcal{R} , which involves evaluating many derivatives and solving a coupled system across the fluid and structural sub-problems. Moreover, if \mathcal{R}_F and \mathcal{R}_S involve discontinuities, some derivatives may not exist.

In this work, we focus on gradient-free optimization methods. Algorithm 1 outlines the general procedure for such methods. The generation of new design candidates in each iteration (Line 9) depends on the specific algorithm employed. For example, in a genetic algorithm, this step involves three operations known as selection, crossover, and mutation, which utilize the values of c , \mathbf{g} , and \mathbf{h} .

In most cases, the FSI problem $\mathcal{R}(\mathbf{w}_F, \mathbf{w}_S; \boldsymbol{\alpha}_i^{(k)}) = \mathbf{0}$ (Line 3 of Algorithm 1) can only be solved approximately using numerical methods. While the discretized fluid and structural governing equations can in principle be solved simultaneously using a monolithic approach [42, 43], partitioned procedures are more commonly adopted as they preserve the modularity of existing CFD and CSD solvers [44, 45]. A basic partitioned procedure can be described as follows. For time step $n = 0, 1, 2, \dots$,

$$\mathbf{W}_F^{n+1} = \widetilde{\mathcal{R}}_F(\mathbf{W}_F^n, \mathbf{W}_S^n), \quad (10)$$

$$\mathbf{W}_S^{n+1} = \widetilde{\mathcal{R}}_S(\mathbf{W}_F^n, \mathbf{W}_S^n; \boldsymbol{\alpha}), \quad (11)$$

where \mathbf{W}_F and \mathbf{W}_S represent the discretized fluid and structural state variables. At each time step, the CSD solver sends the displacement and velocity of its wetted surface (i.e., $\Gamma(t)$) to the CFD solver. These quantities define the fluid boundary position and boundary conditions for the current time step, thereby enforcing the kinematic interface

Algorithm 1 Gradient-Free Optimization of Structures under Fluid-Structure Interaction

Input: Initial design candidates $\alpha_1^{(0)}, \dots, \alpha_M^{(0)}$, maximum optimization iteration N_{iter} , optimization stopping criterion (e.g., change in objective function's value)

- 1: **for** $k = 1, \dots, N_{\text{iter}}$ **do**
- 2: **for** $i = 1, \dots, M$ **do**
- 3: Solve FSI problem $\mathcal{R}(\mathbf{w}_F, \mathbf{w}_S; \alpha_i^{(k)}) = \mathbf{0}$ for \mathbf{w}_F and \mathbf{w}_S .
- 4: Evaluate objective function $c(\mathbf{w}_S, \alpha_i^{(k)})$ and constraints $\mathbf{g}(\mathbf{w}_S, \alpha_i^{(k)})$, $\mathbf{h}(\mathbf{w}_S, \alpha_i^{(k)})$.
- 5: **end for**
- 6: Check stopping criterion. If satisfied,
- 7:
$$\alpha_{\text{opt}} = \arg \min_{\{\alpha_i^{(k)}, i=1, \dots, M\}} \left[c(\mathbf{w}_S, \alpha_i^{(k)}) + \mu \left(\|\max(\mathbf{0}, \mathbf{g}(\mathbf{w}_S, \alpha_i^{(k)}))\|^2 + \|\mathbf{h}(\mathbf{w}_S, \alpha_i^{(k)})\|^2 \right) \right]. \quad \triangleright \mu: \text{penalty factor}$$
- 8: **break**
- 9: Apply a gradient-free update rule to obtain new design candidates $\{\alpha_1^{(k+1)}, \dots, \alpha_M^{(k+1)}\}$.
- 10: **end for**

Output: Final design: α_{opt}

condition (ϕ_1 in (4)). In return, the CFD solver sends the fluid-induced loads (i.e., distributed forces exerted by the fluid on the structure) to the CSD solver, which enforces the dynamic interface condition (ϕ_2 in (7)).

The above description represents a simplified partitioned procedure that assumes a one-step time integrator for both solvers and neglects coupling strategies such as predictor-corrector schemes, sub-iterations, and grid staggering. In the numerical experiments presented in this paper, the CFD solver M2C [46] and the CSD solver Aero-S [47] are coupled through a staggered partitioned procedure in which the fluid and structural time grids are offset by half a time step [45].

2.3. Motivation for current work

The solution of the coupled FSI problem dominates the overall cost of the optimization algorithm. A single CFD–CSD simulation can require on the order of 10^4 CPU core-hours, if not more. Algorithm 1 may require thousands of such analyses. In comparison, the combined cost of all other steps in Algorithm 1 is negligible. As mentioned in Sec. 1, the cost of solving an FSI problem is typically dominated by the fluid sub-problem. In practice, it is not uncommon for the fluid solver to account for over 95% of the total computational cost. Therefore, accelerating the fluid solution—while leaving the structural dynamics solver unchanged—has the potential to yield a substantial speedup in the overall optimization process.

Nonetheless, replacing the high-fidelity CFD solver with a surrogate model introduces errors in the fluid-induced loads. The impact of these errors is problem specific. In the following, we analyze a simple model problem to gain some insight.

Figure 2 shows the geometry of the problem. The structure is an Euler–Bernoulli beam whose cross-sectional area and flexural rigidity are allowed to vary along its length, parameterized by the design variable α . The beam interacts with a fluid flow on one side. The corresponding fluid and structural sub-problems are defined as follows:

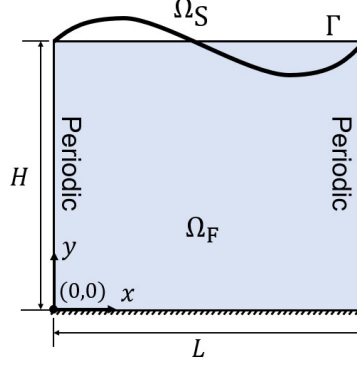


Fig. 2: A two-dimensional fluid-structure interaction model problem.

$$R_F : \begin{cases} \nabla \cdot \mathbf{v} = 0, \\ \rho_F \frac{\partial \mathbf{v}}{\partial t} + \nabla p = 0, \\ p(0, y, t) = p(L, y, t), \\ \frac{\partial p(0, y, t)}{\partial x} = \frac{\partial p(L, y, t)}{\partial x}, \\ \mathbf{v}(x, 0, t) \cdot \mathbf{n} = 0, \\ \mathbf{v}(x, H, t) \cdot \mathbf{n} = \frac{\partial w_S}{\partial t}. \end{cases} \quad R_S : \begin{cases} \rho_S A(x; \alpha) \frac{\partial^2 w}{\partial t^2} + \frac{\partial^2}{\partial x^2} \left(D(x; \alpha) \frac{\partial^2 w}{\partial x^2} \right) = f_{\text{ext}}, \\ w = 0, \quad \frac{\partial^2 w}{\partial x^2} = 0, \quad \text{for } x = 0 \text{ and } x = L, \\ w(x, 0) = w_0 \sin(\pi x/L), \\ \frac{\partial w(x, 0)}{\partial t} = 0, \\ f_{\text{ext}} = b p(x, H, t). \end{cases} \quad (12)$$

To allow analytical solution, the fluid model has been simplified by assuming an incompressible, inviscid, and low-speed flow [48, 13]. While the kinematic interface condition on velocity is enforced, the interface position is assumed to be fixed at $y = H$. Combining the two fluid governing equations, we can eliminate velocity \mathbf{v} to obtain a single Laplace equation for the pressure,

$$\nabla \cdot \nabla p = 0. \quad (13)$$

The boundary conditions can also be expressed in p . In particular, at the fluid-structure interface ($y = H$), the kinematic interface condition becomes

$$\frac{\partial p}{\partial y} = -\rho_F \frac{\partial^2 w}{\partial t^2}. \quad (14)$$

We seek separable solutions of the form

$$w(x, t) = \hat{w}(t)\phi(x), \quad (15)$$

$$p(x, y, t) = \hat{p}(y, t)\phi(x), \quad (16)$$

with $\phi(x) = \sin(\pi x/L)$ to satisfy the initial condition and the periodic boundary conditions. Substituting this ansatz into (13) and its boundary conditions at $y = 0$ and H yields

$$\hat{p}(H, t) = - \underbrace{\frac{\rho_F L}{\pi \tanh(\pi H/L)}}_{:= M_a} \ddot{w}(t), \quad (17)$$

where M_a represents the added mass effect of the fluid. Notably, M_a depends only on the fluid density and geometry, and is independent of the structural design variable α . Integrating the structural governing equation over the spatial domain $0 < x < L$ leads to

$$\bar{M} \ddot{w}(t) + \bar{D} \hat{w}(t) = \hat{p}(H, t), \quad (18)$$

where the effective mass and stiffness are given by

$$\bar{M}(\alpha) = \frac{2}{bL} \int_0^L \rho_S (\phi(x))^2 A(x; \alpha) dx, \quad \bar{D}(\alpha) = \frac{2}{bL} \int_0^L (\phi''(x))^2 D(x; \alpha) dx. \quad (19)$$

Substituting (17) into (18) yields the exact solution for the beam deflection,

$$w_{\text{true}} = w_0 \sin\left(\frac{\pi x}{L}\right) \cos(\omega t), \quad (20)$$

with

$$\omega = \sqrt{\frac{\bar{D}}{\bar{M} + M_a}}. \quad (21)$$

We now consider the scenario in which the structural sub-problem \mathcal{R}_S remains the same, while the fluid sub-problem \mathcal{R}_F is replaced by a surrogate model constructed via localized approximation in the design space. Without loss of generality, we assume that the applied pressure corresponds to the exact solution of the FSI problem evaluated at a nearby design point, α_1 , representing a constant extrapolation in the design space. In this case, the structural equation (18) becomes

$$\bar{M} \ddot{w}(t) + \bar{D} \hat{w}(t) = w_0 M_a \omega_1^2 \cos(\omega_1 t), \quad (22)$$

where $\omega_1 = \sqrt{\bar{D}_1/(\bar{M}_1 + M_a)}$ is the beam's vibration frequency obtained with α_1 . \bar{M}_1 and \bar{D}_1 have the same forms as in (19), with α substituted by α_1 .

Solving (22) yields its exact solution

$$w_{\text{approx}} = w_0 \sin\left(\frac{\pi x}{L}\right) \left[\left(1 - \frac{M_a \omega_1^2}{\bar{D} - \omega_1^2 \bar{M}}\right) \cos(\omega_{\text{dry}} t) + \frac{M_a \omega_1^2}{\bar{D} - \omega_1^2 \bar{M}} \cos(\omega_1 t) \right]. \quad (23)$$

The subscript ‘‘approx’’ indicates that this result is obtained using an approximated (surrogate) fluid pressure. $\omega_{\text{dry}} = \sqrt{\bar{D}/\bar{M}}$ represents the beam's vibration frequency in vacuum.

Thus, the impact of the fluid approximation is characterized by

$$e(\Delta\alpha, t) = \frac{w_{\text{approx}} - w_{\text{true}}}{w_{\text{true}}}, \quad (24)$$

where $\Delta\alpha = \alpha_1 - \alpha$. Given the periodic nature of the solution, we examine the error at early times, as errors neither grow nor decay asymptotically. Applying Taylor series expansion with respect to both $\Delta\alpha$ and t yields

$$e(\Delta\alpha, t) = -\frac{1}{2}t^2 \frac{\gamma}{1+\gamma} \nabla_{\alpha} \left(\frac{\bar{D}}{\bar{M}} \right) \cdot \Delta\alpha + O(\|\Delta\alpha\|^2, t^4), \quad (25)$$

where $\gamma = M_a/\bar{M}$ denotes the ratio of fluid added mass to the structural mass.

Equation (25) has several implications that justify the use of surrogate fluid models based on interpolation in the design space. As expected, the leading-order error increases monotonically with the magnitude of the fluid's added mass effect. When the ratio γ is small—for example, when the fluid density ρ_F is much smaller than the structural density ρ_S —the error tends to zero in the limit $\gamma \rightarrow 0$. Moreover, the factor $\gamma/(1+\gamma)$ is strictly concave and bounded by 1. Therefore, even for problems that exhibit strong added mass effect, the error induced by the surrogate fluid model remains bounded and is proportional to $\Delta\alpha$.

3. An Adaptive Multi-Fidelity Optimization Framework

We introduce an interpolation-based surrogate model to approximate the fluid-induced loads at the fluid-structure interface. This approximation is used alongside the original CFD model during the optimization process, while the structural sub-problem \mathcal{R}_S is always solved using the high-fidelity CSD solver. A decision model is developed to estimate the approximation error. For each design point evaluation requested by the optimization algorithm, the decision model selects between a coupled CFD–CSD analysis and a CSD-only analysis with fluid loads computed using the surrogate model. Whenever a coupled analysis is performed, the fluid result is used to adaptively improve the accuracy of the surrogate model and to refine the decision model.

3.1. Approximation of fluid-induced loads

During the optimization process, suppose that coupled CFD–CSD analyses have been performed for a set of structural designs. The corresponding fluid solutions are stored and treated as ground-truth data. To approximate the fluid pressure for evaluating a new design α_* , we construct a local, dimension-by-dimension interpolation surrogate of the form

$$\tilde{p}(\mathbf{x}, t_n; \alpha_*) = \sum_{k=1}^{N_b} w_k^{(\alpha)} \left[\sum_{i=0,1} w_{k,i}^{(t)} \left(\sum_j w_{k,i,j}^{(x)} p(\mathbf{x}_j, t_{n_k+i}; \alpha_k) \right) \right], \quad (26)$$

where \mathbf{x} denotes the Eulerian coordinates of a point on the discretized fluid-structure interface, such as a node or Gauss point. t_n is a time step of the CSD solver. The quantity $p(\mathbf{x}_j, t_{n_k+i}; \alpha_k)$ represents the pressure obtained from the coupled analysis for design α_k , at spatial location (e.g., a node) \mathbf{x}_j and time step t_{n_k+i} . The coefficients $w^{(\alpha)}$, $w^{(t)}$, and $w^{(x)}$ denote the interpolation weights in the design space, temporal domain, and spatial domain, respectively.

In the design space, all design variables are first normalized to allow consistent distance measures across different dimensions. For the new design α_* , we identify its N_b nearest neighbors from the set of previously evaluated designs,

denoted by $\alpha_k, k = 1, \dots, N_b$. N_b can be prescribed directly or determined by a cut-off distance. A common approach for interpolating unstructured data is radial basis function (RBF) interpolation, in which the weights are obtained as

$$w_k^{(\alpha)} = \sum_{m=1}^{N_b} \phi(\|\alpha_* - \alpha_m\|) (\mathbf{\Phi}^{-1})_{mk}, \quad (27)$$

where $\|\cdot\|$ denotes the Euclidean norm, $\phi(\cdot)$ is a radial basis function, and $\mathbf{\Phi} \in \mathbb{R}^{N_b \times N_b}$ is the interpolation matrix with entries $[\mathbf{\Phi}]_{ij} = \phi(\|\alpha_i - \alpha_j\|)$.

However, standard RBF interpolation does not enforce positivity or boundedness of the interpolation weights. In practice, we have observed that during the early iterations of the optimization process when the available data are sparsely distributed, the query design point α_* often lies outside the convex hull of the sampled designs. In such cases, RBF interpolation can produce negative or high-magnitude weights, leading to large errors.

To avoid this issue, we instead adopt a normalized distance-based interpolation scheme:

$$w_k^{(\alpha)} = \frac{\phi(\|\alpha_* - \alpha_k\|)}{\sum_{m=1}^{N_b} \phi(\|\alpha_* - \alpha_m\|)}. \quad (28)$$

This formulation guarantees that all interpolation weights are non-negative and collectively sum to unity, providing a convex combination of the neighbor values. When the query design α_* lies outside the region spanned by the neighbors, the scheme naturally assigns the highest weight to the nearest neighbor. The choice of radial basis function ϕ can vary, with common options including multi-quadratic functions, inverse multi-quadratic functions, thin-plate splines, and Gaussian functions. In the numerical tests presented in this paper, we use the Gaussian functions, given by

$$\phi(\|\alpha_* - \alpha_k\|) = \exp\left(-\frac{\|\alpha_* - \alpha_k\|^2}{2l^2}\right), \quad (29)$$

where l is a scaling factor, set in this work to be slightly larger than the maximum distance between design points that have been evaluated with coupled analysis.

The temporal interpolation is performed using a first-order linear scheme. In (26), n_k denotes the time-step index from the coupled analysis for design α_k that satisfies $t_{n_k} \leq t_n < t_{n_k+1}$. The weights $w_{k,0}^{(t)}$ and $w_{k,1}^{(t)}$ are given by

$$w_{k,i}^{(t)} = \frac{|t_n - t_{n_k+1-i}|}{t_{n_k+1} - t_{n_k}}, \quad i = 0, 1. \quad (30)$$

The spatial interpolation needs to properly account for the mismatches between different coordinate systems. In a coupled analysis, fluid variables such as pressure are computed at nodes (or cell centers) of an Eulerian mesh, which generally do not coincide with the nodes or Gauss points of the Lagrangian structural mesh. Moreover, the structural geometry may vary across different designs (e.g., α_* and α_k), leading to discrepancies in the Lagrangian coordinates of the interface.

A straightforward approach is to perform the interpolation entirely in the Eulerian reference frame by directly applying (26), with \mathbf{x}_j being fluid nodes from the coupled analysis for design α_k that lie in the vicinity of the interface point \mathbf{x} . This approach has a clear drawback, as illustrated in Fig. 3. The figure shows the structural mesh of the

query design α_* overlaid with both the fluid and structural meshes corresponding to a nearby design α_k used in the interpolation. Computing the pressure at x involves interpolating values from nearby nodes on the fluid mesh, such as those labeled x_1 and x_2 . In the coupled analysis for design α_k , these nodes lie beneath the structure, near its lower surface, whereas in the query design the point x is located on the upper surface. In other words, this would result in using fluid pressure on the wrong side of the structure.

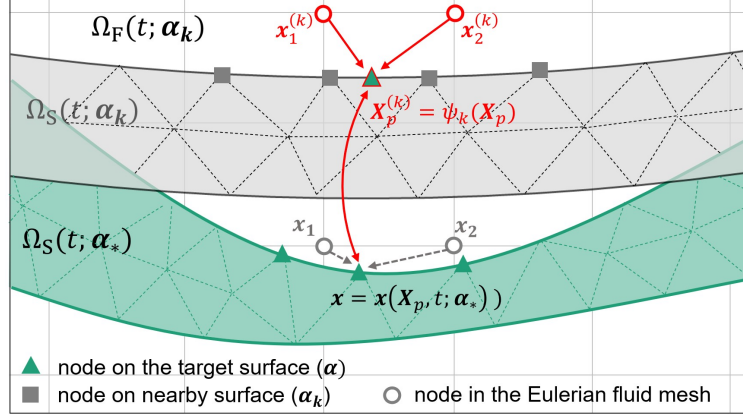


Fig. 3: Illustration of spatial interpolation across different structural designs and between Eulerian fluid and Lagrangian structural reference frames.

In this work, spatial interpolation is performed using both Lagrangian and Eulerian coordinates. For each neighboring design α_k , we define a function

$$\mathbf{X}^{(k)} = \psi_k(\mathbf{X}) \quad (31)$$

that maps $\Gamma(0; \alpha_*)$ to $\Gamma(0; \alpha_k)$ using Lagrangian coordinates. ψ_k is expected to be continuous in \mathbf{X} . Furthermore, when all such functions are considered collectively as a function of the design variables, i.e., $\psi_k(\mathbf{X}) = \Psi(\alpha_k, \mathbf{X})$, its dependence on α is also expected to be continuous. As long as the design space does not involve topological changes to the interface geometry (i.e., the interfaces associated with all designs are homeomorphic), such functions exist and are usually straightforward to construct. For example, if the interface geometry remains unchanged across designs, ψ_k reduces to the identity map. For designs involving shape changes—e.g., evolving from a sphere to an oval—the shape transformation itself defines Ψ . As illustrated in Fig. 3, the continuity requirements ensure that ψ_k maps a point \mathbf{X}_p on the lower surface of the query design α^* to a point on the lower surface of α_k .

Once $\mathbf{X}^{(k)}$ is identified, its corresponding position, $\mathbf{x}(\mathbf{X}^{(k)}, t_{n_k+i}; \alpha_k)$, is readily available from the structural displacement field provided by the coupled analysis for design α_k . The pressure at this location is then evaluated by interpolating from nearby nodes on the fluid mesh, such as those labeled $x_1^{(k)}$ and $x_2^{(k)}$. This interpolation can be performed using either the fluid mesh, or through an unstructured, distance-based approach similar to that used in the design space. The chosen strategy defines the spatial interpolation weights $w^{(x)}$.

Incorporating the mapping ψ_k , the pressure approximation in (26) is rewritten as

$$\tilde{p}(\mathbf{X}, t_n; \boldsymbol{\alpha}_*) = \sum_{k=1}^{N_b} w_k^{(\alpha)} \left(\sum_{i=0,1} w_{k,i}^{(t)} \tilde{p}(\psi_k(\mathbf{X}), t_{n_k+i}; \boldsymbol{\alpha}_k) \right), \quad (32)$$

with

$$\tilde{p}(\psi_k(\mathbf{X}), t_{n_k+i}; \boldsymbol{\alpha}_k) = \sum_{j=1}^{N_p} w_{k,i,j}^{(x)} p(\mathbf{x}_j, t_{n_k+i}; \boldsymbol{\alpha}_k). \quad (33)$$

Here, \mathbf{x}_j , $j = 1, \dots, N_p$, denote the fluid mesh nodes used to interpolate pressure at $\mathbf{x}(\mathbf{X}^{(k)}, t_{n_k+i}; \boldsymbol{\alpha}_k)$. Once \tilde{p} is computed, the distributed loads are obtained by integrating \tilde{p} on the structural surface with finite element basis functions.

This method can be extended to fluid flows with viscous shear forces by approximating the surface traction vector \mathbf{T} instead of pressure p . However, simply replacing p by \mathbf{T} in (32) and (33) is not sufficient. Different structural designs generally have different surface orientations and normal directions at corresponding material points. Because the interpolation weights $w_k^{(\alpha)}$ are obtained solely from distances in the design space, they do not account for these geometric discrepancies. For example, consider a problem where the structure experiences purely normal traction (i.e., no shear). Suppose the query design $\boldsymbol{\alpha}_*$ has two neighbors, $\boldsymbol{\alpha}_1$ and $\boldsymbol{\alpha}_2$, with surface normals \mathbf{n}_1 and \mathbf{n}_2 that differ from the query design's surface normal \mathbf{n}_* . Direct interpolation in a global coordinate frame yields

$$\tilde{\mathbf{T}}(\mathbf{X}, t; \boldsymbol{\alpha}_*) = w_1^{(\alpha)} \left[\sum_{i=0,1} w_{k,i}^{(t)} \left(\sum_j w_{k,i,j}^{(x)} p(\mathbf{x}_j, t_{n_k+i}; \boldsymbol{\alpha}_1) \right) \right] \mathbf{n}_1 + w_2^{(\alpha)} \left[\sum_{i=0,1} w_{k,i}^{(t)} \left(\sum_j w_{k,i,j}^{(x)} p(\mathbf{x}_j, t_{n_k+i}; \boldsymbol{\alpha}_2) \right) \right] \mathbf{n}_2, \quad (34)$$

which, in general, is not aligned with \mathbf{n}_* , and therefore introducing a spurious tangential component.

To avoid this issue, we decompose the traction vector at each neighboring design into scalar components relative to a local orthonormal basis. These components physically represent the normal and tangential stresses in the local basis. Each scalar component is then interpolated separately, and the traction is then reconstructed using the local basis of the query design (Fig. 4), effectively making the interpolation independent of geometric differences between structural designs.

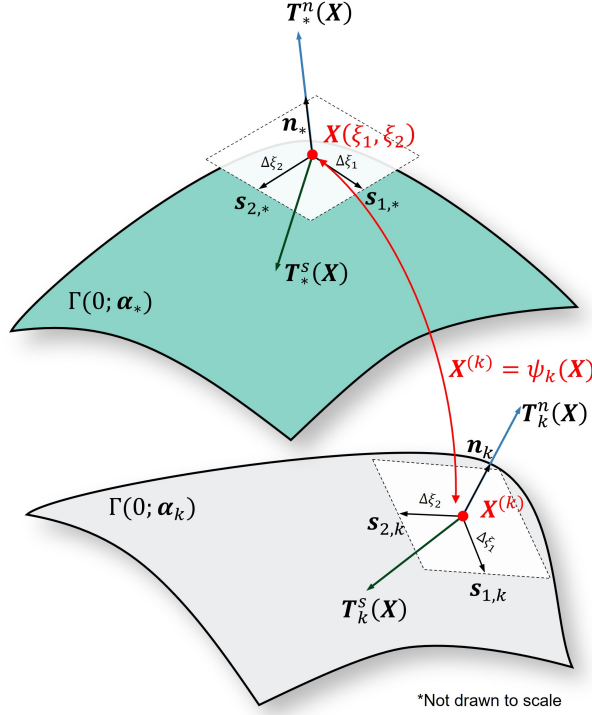


Fig. 4: Illustration of the local orthonormal basis used for traction decomposition across structural designs. The normal traction component $T^n(\mathbf{X}, t, \boldsymbol{\alpha}) = T^n \mathbf{n}$ acts perpendicular to the surface, while the shear traction component $T^n(\mathbf{X}, t, \boldsymbol{\alpha}) = T^n \mathbf{n}$ and $T^s(\mathbf{X}, t, \boldsymbol{\alpha}) = T^{s_1} s_1 + T^{s_2} s_2$ lies in the local tangent plane. Collectively, $\mathbf{T} = \mathbf{T}^n + \mathbf{T}^s$.

The local orthonormal basis comprises the surface normal \mathbf{n} and two tangent vectors, s_1 and s_2 , defined on the tangent plane of the fluid-structure interface. While the surface normal is directly available from the geometry, the tangent vectors must be determined. Let (ξ_1, ξ_2) be parametric coordinates on the reference interface $\Gamma(0; \alpha_*)$, with $\mathbf{X} = \mathbf{X}(\xi_1, \xi_2)$. We define the neighboring material points in each parametric direction as

$$\mathbf{X}^{+1} = \mathbf{X}(\xi_1 + \Delta\xi_1, \xi_2), \quad \mathbf{X}^{+2} = \mathbf{X}(\xi_1, \xi_2 + \Delta\xi_2). \quad (35)$$

For a neighboring design α_k , the two tangent vectors at the mapped point $\psi_k(\mathbf{X})$ are defined as

$$s_i(\psi_k(\mathbf{X}), t; \alpha_k) = \frac{\mathbf{x}(\psi_k(\mathbf{X}^{+i}), t; \alpha_k) - \mathbf{x}(\psi_k(\mathbf{X}), t; \alpha_k)}{\|\mathbf{x}(\psi_k(\mathbf{X}^{+i}), t; \alpha_k) - \mathbf{x}(\psi_k(\mathbf{X}), t; \alpha_k)\|}, \quad i = 1, 2, \quad (36)$$

where $\mathbf{x}(\mathbf{X}, t; \boldsymbol{\alpha})$ denotes the spatial position of material point \mathbf{X} at time t for design $\boldsymbol{\alpha}$. Similarly, the tangent vectors for the query design are

$$s_i(\mathbf{X}, t; \alpha_*) = \frac{\mathbf{x}(\mathbf{X}^{+i}, t; \alpha_*) - \mathbf{x}(\mathbf{X}, t; \alpha_*)}{\|\mathbf{x}(\mathbf{X}^{+i}, t; \alpha_*) - \mathbf{x}(\mathbf{X}, t; \alpha_*)\|}, \quad i = 1, 2. \quad (37)$$

Using this local basis, the traction vector at each neighbor is decomposed as

$$\mathbf{T}(\psi_k(\mathbf{X}), t; \alpha_k) = T_k^n \mathbf{n}_k + T_k^{s_1} s_{1,k} + T_k^{s_2} s_{2,k}, \quad (38)$$

where T_k^n , $T_k^{s_1}$, and $T_k^{s_2}$ are the scalar components of the traction in the normal and tangential directions, respectively, with $\mathbf{n}_k = \mathbf{n}(\psi_k(\mathbf{X}), t; \boldsymbol{\alpha}_k)$ and $s_{i,k} = s(\psi_k(\mathbf{X}), t; \boldsymbol{\alpha}_k)$.

The traction components for a new structural design $\boldsymbol{\alpha}_*$ are approximated by interpolating each scalar component separately using the normalized distance-based interpolation, i.e.,

$$\tilde{T}^\chi(\mathbf{X}, t_n; \boldsymbol{\alpha}_*) = \sum_{k=1}^{N_b} w_k^{(\alpha)} \left(\sum_{i=0,1} w_{k,i}^{(t)} \tilde{T}^\chi(\psi_k(\mathbf{X}), t_{n_k+i}; \boldsymbol{\alpha}_k) \right), \quad \chi = n, s_1, s_2, \quad (39)$$

with

$$\tilde{T}^\chi(\psi_k(\mathbf{X}), t_{n_k+i}; \boldsymbol{\alpha}_k) = \sum_{j=1}^{N_p} w_{k,i,j}^{(x)} T^\chi(\mathbf{x}_j, t_{n_k+i}; \boldsymbol{\alpha}_k). \quad (40)$$

The approximate traction vector is then reconstructed using the local basis of the query design:

$$\tilde{\mathbf{T}}(\mathbf{X}, t; \boldsymbol{\alpha}_*) = \tilde{T}^n \mathbf{n}_* + \tilde{T}^{s_1} \mathbf{s}_{1,*} + \tilde{T}^{s_2} \mathbf{s}_{2,*}, \quad (41)$$

where $\mathbf{n}_* = \mathbf{n}(\mathbf{X}, t; \boldsymbol{\alpha}_*)$ and $\mathbf{s}_{i,*} = \mathbf{s}_i(\mathbf{X}, t; \boldsymbol{\alpha}_*)$.

For fluid flows that only exert a pressure on the fluid-structure interface, $T^n = p$ and $T^{s_1} = T^{s_2} = 0$. Substituting these in (39) and (40) recovers the pressure approximation given by (32).

3.2. Adaptive decision model

We develop an adaptive decision model based on Gaussian process regression (GPR) to estimate the accuracy of the surrogate model introduced in the previous subsection. Assuming the fluid-induced loads are computed using pressure only (i.e., (32)), we define the approximation error as

$$e(\boldsymbol{\alpha}) = \frac{1}{N_t} \sum_{n=1}^{N_t} \frac{\|p(\mathbf{X}, t^n; \boldsymbol{\alpha}) - \tilde{p}(\mathbf{X}, t^n; \boldsymbol{\alpha})\|}{\|p(\mathbf{X}, t^n; \boldsymbol{\alpha})\|}, \quad (42)$$

where p and \tilde{p} denote the fluid pressure field generated by coupled CFD-CSD analysis and the surrogate model, respectively. $\|\cdot\|$ denotes the function L^2 norm over the spatial domain of \mathbf{X} . N_t is the total number of time steps. Equation (42) can be extended to the traction approximation in (39) by generalizing the norm to vector-valued functions.

Let $\mathcal{A} = \{\boldsymbol{\alpha}_1, \boldsymbol{\alpha}_2, \dots, \boldsymbol{\alpha}_{N_{\text{true}}}\}$ denote the set of structural designs that have been evaluated using coupled CFD-CSD analyses. For each design $\boldsymbol{\alpha}_k \in \mathcal{A}$, we compute the approximate pressure field \tilde{p} using the surrogate model and evaluate its error, $e_k = e(\boldsymbol{\alpha}_k)$, by (42). These values are denoted collectively by vector $\mathbf{e} = [e_1, e_2, \dots, e_{N_{\text{true}}}]^T$. The regression dataset is then given by

$$\mathcal{D} = \{(\boldsymbol{\alpha}_1, e_1), (\boldsymbol{\alpha}_2, e_2), \dots, (\boldsymbol{\alpha}_{N_{\text{true}}}, e_{N_{\text{true}}})\}. \quad (43)$$

To predict the error at a new design point $\boldsymbol{\alpha}_*$, we employ the regression model

$$e(\boldsymbol{\alpha}) = \mathbf{y}(\boldsymbol{\alpha})^T \boldsymbol{\beta} + f(\boldsymbol{\alpha}). \quad (44)$$

The first term, $\mathbf{y}(\boldsymbol{\alpha})^T \boldsymbol{\beta}$, captures the global trend in the dataset \mathcal{D} while the second term, $f(\boldsymbol{\alpha})$, models the local deviations from this trend. Here, $\mathbf{y}(\boldsymbol{\alpha})$ is chosen to be a set of low-order polynomial basis functions and $\boldsymbol{\beta}$ their corresponding coefficients. For example, if $\boldsymbol{\alpha} = [\alpha_{(1)}, \alpha_{(2)}]^T \in \mathbb{R}^2$, a second-order polynomial basis is given by $\mathbf{y} = [1, \alpha_{(1)}, \alpha_{(2)}, \alpha_{(1)}^2, \alpha_{(2)}^2, \alpha_{(1)}\alpha_{(2)}]^T$. The local deviation term is modeled using a Gaussian process (GP) with zero mean and a covariance function $k(\boldsymbol{\alpha}, \boldsymbol{\alpha}')$, i.e.,

$$f(\boldsymbol{\alpha}) \sim GP(0, k(\boldsymbol{\alpha}, \boldsymbol{\alpha}')). \quad (45)$$

By definition, a Gaussian process implies that any finite collection of function evaluations (here, f) follows a joint Gaussian distribution [49]. Consequently, the training error vector \mathbf{e} and the error at the test point $e_* = e(\boldsymbol{\alpha}_*)$ satisfy

$$\begin{bmatrix} \mathbf{e} \\ e_* \end{bmatrix} \Big| \mathcal{A}, \boldsymbol{\beta} \sim \mathcal{N} \left(\begin{bmatrix} \mathbf{Y}^T \boldsymbol{\beta} \\ \mathbf{y}_*^T \boldsymbol{\beta} \end{bmatrix}, \begin{bmatrix} \mathbf{K} & \mathbf{k}_* \\ \mathbf{k}_*^T & k_{**} \end{bmatrix} \right), \quad (46)$$

where $\mathbf{Y} = [\mathbf{y}(\boldsymbol{\alpha}_1), \mathbf{y}(\boldsymbol{\alpha}_2), \dots, \mathbf{y}(\boldsymbol{\alpha}_{N_{\text{true}}})]$ collects the basis vectors \mathbf{y} evaluated at training points, and $\mathbf{y}_* = \mathbf{y}(\boldsymbol{\alpha}_*)$. The covariance matrix $\mathbf{K} \in \mathbb{R}^{N_{\text{true}} \times N_{\text{true}}}$ has entries

$$[\mathbf{K}]_{ij} = k(\boldsymbol{\alpha}_i, \boldsymbol{\alpha}_j) + \sigma_m^2 \delta_{ij}, \quad (47)$$

where σ_m^2 is the measurement noise variance, and δ_{ij} is the Kronecker delta. \mathbf{k}_* is the cross-covariance vector, given by $\mathbf{k}_* = [k(\boldsymbol{\alpha}_*, \boldsymbol{\alpha}_1), k(\boldsymbol{\alpha}_*, \boldsymbol{\alpha}_2), \dots, k(\boldsymbol{\alpha}_*, \boldsymbol{\alpha}_{N_{\text{true}}})]^T$. $k_{**} = k(\boldsymbol{\alpha}_*, \boldsymbol{\alpha}_*)$ is the prior variance at $\boldsymbol{\alpha}_*$.

Conditioning the joint distribution in (46) yields the following posterior distribution for e_* :

$$e_* \Big| \mathcal{A}, \mathbf{e}, \boldsymbol{\beta} \sim \mathcal{N} \left(\mathbf{y}_*^T \boldsymbol{\beta} + \mathbf{k}_*^T \mathbf{K}^{-1} (\mathbf{e} - \mathbf{Y}^T \boldsymbol{\beta}), k_{**} - \mathbf{k}_*^T \mathbf{K}^{-1} \mathbf{k}_* \right). \quad (48)$$

By this distribution, the error e_* depends on the choice of the covariance function $k(\cdot, \cdot)$, the measurement variance σ_m^2 , and the polynomial coefficients $\boldsymbol{\beta}$. We treat $\boldsymbol{\beta}$ as an uncertain parameter and assign it a Gaussian prior, namely $\boldsymbol{\beta} \sim \mathcal{N}(\mathbf{b}, \mathbf{B})$. This treatment allows the model to account for parameter uncertainty, which is particularly important when the training dataset \mathcal{D} is small during the early iterations of the optimization. By Bayes' theorem, the posterior distribution of $\boldsymbol{\beta}$ is given by

$$\boldsymbol{\beta} \Big| \mathcal{A}, \mathbf{e} \sim \mathcal{N} \left((\mathbf{B}^{-1} + \mathbf{Y} \mathbf{K}^{-1} \mathbf{Y}^T)^{-1} (\mathbf{Y} \mathbf{K}^{-1} \mathbf{e} + \mathbf{B}^{-1} \mathbf{b}), (\mathbf{B}^{-1} + \mathbf{Y} \mathbf{K}^{-1} \mathbf{Y}^T)^{-1} \right). \quad (49)$$

In this work, no prior information is available regarding the trend of the approximation error before the optimization begins. To reflect this in the model formulation, we adopt a vague prior by taking $\mathbf{B}^{-1} \rightarrow \mathbf{0}$. In this limit, the prior distribution has no influence on the posterior inference of $\boldsymbol{\beta}$, so that their posterior distribution is completely determined by the dataset \mathcal{D} . This data-driven treatment is further justified in the present context because the approximation error defined in (42) depends on problem-specific factors—such as the sensitivity of the fluid loads to structural design variables—that is unknown *a priori*. Under the non-informative prior, the posterior mean of $\boldsymbol{\beta}$ reduces to

$$\bar{\boldsymbol{\beta}} \equiv \mathbb{E}[\boldsymbol{\beta} \Big| \mathcal{A}, \mathbf{e}] = (\mathbf{Y} \mathbf{K}^{-1} \mathbf{Y}^T)^{-1} (\mathbf{Y} \mathbf{K}^{-1} \mathbf{e}). \quad (50)$$

We marginalize the predictive distribution over the posterior distribution of $\boldsymbol{\beta}$. By (48), (49), and (50), we obtain a Gaussian distribution for e_* conditional on only the data set \mathcal{D} , with mean and variance given by

$$\mathbb{E}[e_* | \mathcal{A}, \mathbf{e}] = \mathbb{E}_{\boldsymbol{\beta}}[\mathbb{E}[e_* | \mathcal{A}, \mathbf{e}, \boldsymbol{\beta}]] = \mathbf{y}_*^T \bar{\boldsymbol{\beta}} + \mathbf{k}_*^T \mathbf{K}^{-1}(\mathbf{e} - \mathbf{Y}^T \bar{\boldsymbol{\beta}}), \quad (51a)$$

$$\begin{aligned} \mathbb{V}[e_* | \mathcal{A}, \mathbf{e}] &= \mathbb{E}_{\boldsymbol{\beta}}[\mathbb{V}[e_* | \mathcal{A}, \mathbf{e}, \boldsymbol{\beta}]] + \mathbb{V}_{\boldsymbol{\beta}}[\mathbb{E}[e_* | \mathcal{A}, \mathbf{e}, \boldsymbol{\beta}]] \\ &= k_{**} - \mathbf{k}_*^T \mathbf{K}^{-1} \mathbf{k}_* + (\mathbf{y}_* - \mathbf{Y} \mathbf{K}^{-1} \mathbf{k}_*)^T (\mathbf{Y} \mathbf{K}^{-1} \mathbf{Y}^T)^{-1} (\mathbf{y}_* - \mathbf{Y} \mathbf{K}^{-1} \mathbf{k}_*). \end{aligned} \quad (51b)$$

This marginalization allows the resulting predictive variance to account for not only the intrinsic uncertainty of the Gaussian process but also the uncertainty in $\boldsymbol{\beta}$. $\mathbb{E}[e_* | \mathcal{A}, \mathbf{e}]$ provides an estimate of the surrogate model's error for structural design $\boldsymbol{\alpha}_*$, while the corresponding uncertainty is quantified by the standard deviation

$$u_* = \sqrt{\mathbb{V}[e_* | \mathcal{A}, \mathbf{e}]}. \quad (52)$$

The covariance function is chosen to be the squared exponential function,

$$k(\boldsymbol{\alpha}, \boldsymbol{\alpha}') = \sigma^2 \exp\left(-\frac{1}{2}(\boldsymbol{\alpha} - \boldsymbol{\alpha}')^T \boldsymbol{\Theta}(\boldsymbol{\alpha} - \boldsymbol{\alpha}')\right), \quad (53)$$

where $\boldsymbol{\Theta} = \text{diag}(\theta_1, \dots, \theta_d)$ is a diagonal matrix containing the inverse length-scale parameters associated with each design variable dimension, and σ^2 is the kernel variance.

The parameters σ_m^2 , $\{\theta_i\}_{i=1}^d$, and σ^2 are determined by maximizing the logarithmic marginal likelihood of the observed dataset \mathcal{D} . Under the assumption of a non-informative prior for $\boldsymbol{\beta}$,

$$p(\mathbf{e} | \mathcal{A}) = \frac{1}{\sqrt{(2\pi)^{N_{\text{true}} - N_{\boldsymbol{\beta}}} |\mathbf{K}| |\mathbf{Y} \mathbf{K}^{-1} \mathbf{Y}^T|}} \exp\left(-\frac{1}{2}(\mathbf{e} - \mathbf{Y}^T \bar{\boldsymbol{\beta}})^T \mathbf{K}^{-1}(\mathbf{e} - \mathbf{Y}^T \bar{\boldsymbol{\beta}})\right), \quad (54)$$

where $N_{\boldsymbol{\beta}}$ denotes the dimension of $\boldsymbol{\beta}$, that is, the number of polynomial basis functions in \mathbf{y} . Maximizing the logarithmic likelihood yields

$$\{\sigma_m^2, \{\theta_i\}_{i=1}^d, \sigma^2\} = \arg \max \left(-\frac{1}{2}(\mathbf{e} - \mathbf{Y}^T \bar{\boldsymbol{\beta}})^T \mathbf{K}^{-1}(\mathbf{e} - \mathbf{Y}^T \bar{\boldsymbol{\beta}}) - \frac{1}{2} \log |\mathbf{K}| - \frac{1}{2} \log |\mathbf{Y} \mathbf{K}^{-1} \mathbf{Y}^T| \right). \quad (55)$$

This unconstrained optimization problem can be solved numerically using gradient-based methods.

With the regression model in place, the selection between the CFD solver and the surrogate model is based on whether the predicted error and its associated uncertainty satisfy user-specified tolerances τ_e and τ_u . Specifically, we adopt a three-standard-deviation upper confidence bound, corresponding to a 99.7% confidence level, and accept the surrogate model when

$$3u_* \leq \tau_u, \quad (56)$$

and

$$\mathbb{E}[e_* | \mathcal{A}, \mathbf{e}] \leq \tau_e. \quad (57)$$

When both criteria are satisfied, the surrogate model replaces the CFD solver and provides the fluid-induced load to the CSD solver for evaluating the structural design $\boldsymbol{\alpha}_*$. Otherwise, the framework reverts to the coupled CFD–CSD analysis (11), and the resulting fluid solution is used to augment the dataset \mathcal{D} .

Remark: For the GPR model to be well-defined, the equations (50) and (51b) require the matrix $\mathbf{Y}\mathbf{K}^{-1}\mathbf{Y}^T \in \mathbb{R}^{N_\beta \times N_\beta}$ to be invertible. Since \mathbf{K} is the covariance matrix with added measurement noise ($\sigma_m^2 > 0$), it is symmetric and positive definite, implying that \mathbf{K}^{-1} exists and is also symmetric and positive definite. Using the Cholesky factorization of \mathbf{K}^{-1} one can show that $\text{rank}(\mathbf{Y}\mathbf{K}^{-1}\mathbf{Y}^T) = \text{rank}(\mathbf{Y}) \leq \min(N_\beta, N_{\text{true}})$. Full rank, and hence invertibility, therefore requires $N_{\text{true}} \geq N_\beta$. For a polynomial basis of order p in a d -dimensional design space, $N_\beta = \binom{d+p}{p}$, meaning at least this many high-fidelity CFD–CSD evaluations must be available before the decision model can be constructed.

4. Implementation

4.1. Baseline optimization framework

We begin by describing an implementation of the optimization process summarized in Algorithm 1, in which all design points are evaluated using coupled CFD–CSD analysis. This implementation serves as a baseline for the adaptive multi-fidelity framework, and is used to generate reference results for performance assessment. The framework consists of four major components that exchange data in real-time: a numerical optimizer, a mesh generator, a CFD solver, and a CSD solver.

Figure 5 illustrates the workflow. The iterative optimization steps are shaded in gray, and the major components are highlighted in bold. The resulting software framework is named *SOFICS* (Structural Optimization through Fluid–structure Interaction and Coupled Simulations). The optimization loop is driven by the open-source C++ toolkit Dakota (Design Analysis Kit for Optimization and Terascale Applications) [50], which provides a variety of gradient-free algorithms along with asynchronous and parallel evaluation capabilities.

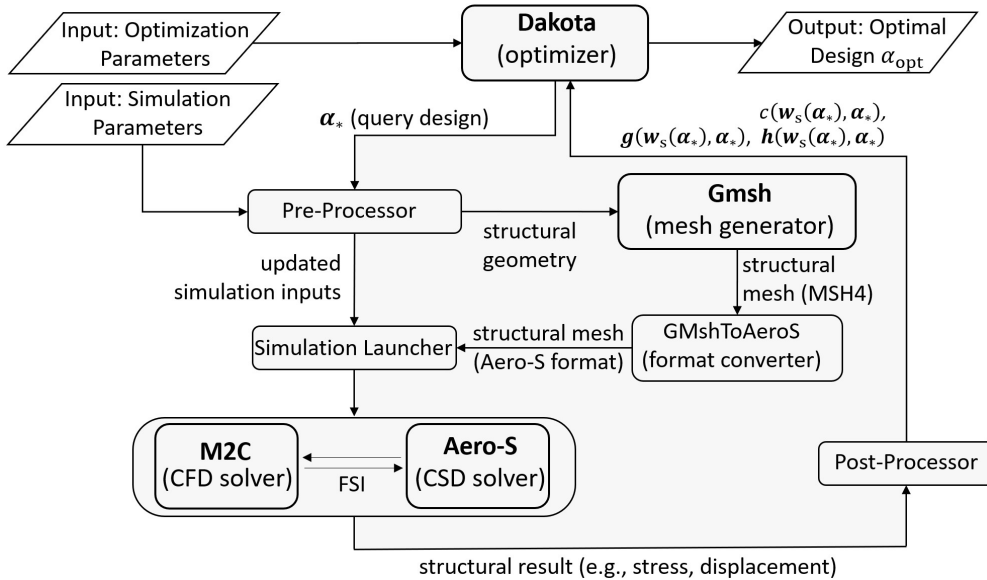


Fig. 5: Implementation of the baseline optimization framework (SOFICS-Base).

The fluid and structural sub-problems in (11) are solved using the CFD solver M2C and the CSD solver Aero-S, respectively. M2C is an Eulerian finite volume compressible flow solver, equipped with an embedded boundary method for FSI [46]. Aero-S is a Lagrangian finite element solver for structural and solid dynamics, supporting finite deformations and nonlinear material behaviors (e.g., plasticity, hyperelasticity, and viscoelasticity) [47]. The two solvers are both written in C++, and are coupled using a partitioned procedure and the FIVER (FInite Volume method based on Exact multi-material Riemann problems) method [11, 51].

For each new structural design α_* , Dakota interfaces with the fluid and structural solvers through a Bash-based pre-processor. The pre-processor updates the simulation input files and calls the open-source meshing tool Gmsh [52] to create a new structural mesh. Because of the use of embedded boundary method, the fluid mesh can be the same for all design evaluations. Next, a simulation launcher executes the coupled analysis on a computer cluster. Upon completion, the results from Aero-S are post-processed to evaluate the objective function c and the constraints \mathbf{g} and \mathbf{h} .

The simulation launcher in SOFICS is designed to request a single allocation (i.e., fixed CPU cores and wall time) for the entire optimization process. Within this allocation, it runs coupled analysis concurrently and continuously using any available resources. This approach avoids delays and resource idleness associated with repeated queue submissions.

4.2. Adaptive multi-fidelity framework

The multi-fidelity optimization framework described in Sec. 3.2 is implemented by extending the baseline optimization workflow, as summarized in Algorithm 2. The design population management remains unchanged. The modifications primarily lie in the evaluation of individual candidate designs and the update of the decision model.

Algorithm 2 Adaptive Multi-Fidelity Structural Optimization under Fluid-Structure Interaction

Input: Initial design candidates $\alpha_1^{(0)}, \dots, \alpha_M^{(0)}$, maximum optimization iteration N_{iter} , optimization stopping criterion

(e.g., change in objective function's value), penalty factory μ , tolerances τ_e and τ_u , and number of neighbors N_b

```
1: Set  $\mathcal{D} = \emptyset, \mathcal{A} = \emptyset$ .
2: for  $k = 1, \dots, N_{\text{iter}}$  do
3:   Set  $N_{\text{true}} = |\mathcal{A}|$ .
4:   Part 1: Multi-fidelity analysis
5:   for  $i = 1, \dots, M$  do
6:      $\alpha_* \leftarrow \alpha_i^{(k)}$ 
7:     accept_surrogate  $\leftarrow$  false
8:     if  $N_{\text{true}} \geq N_b$  then
9:       Compute  $\mathbf{y}_*, \mathbf{k}_*$ , and  $k_{**}$  as defined in Sec. 3.2.
10:      Evaluate  $\mathbb{E}[e_* | \mathcal{A}, \mathbf{e}]$  by (51a) and  $u_*$  by (51b) and (52).
11:       if  $3u_* \leq \tau_u$  and  $\mathbb{E}[e_* | \mathcal{A}, \mathbf{e}] \leq \tau_e$  then
12:         accept_surrogate  $\leftarrow$  true
13:       end if
14:     end if
15:     if accept_surrogate then
16:       Identify nearest neighbors  $\{\alpha_1, \dots, \alpha_{N_b}\} \subset \mathcal{A}$  of  $\alpha_*$  such that,
17:         
$$\|\alpha_* - \alpha_1\| \leq \dots \leq \|\alpha_* - \alpha_{N_b}\| \leq \|\alpha_* - \alpha'\|, \quad \forall \alpha' \in \mathcal{A} \setminus \{\alpha_1, \dots, \alpha_{N_b}\}.$$

18:       Solve structural sub-problem  $\mathcal{R}_S(\tilde{p}, \mathbf{w}_S; \alpha_*) = \mathbf{0}$  for  $\mathbf{w}_S$  with boundary condition
19:         
$$\phi_2 = (\sigma_S - \tilde{p}(X, t; \alpha_*)\mathbb{I}) \cdot \mathbf{n} = \mathbf{0}, \quad (\text{cf. (8)})$$

20:       where  $\tilde{p}$  is computed using the surrogate model (32).
21:     else
22:       Solve coupled FSI problem  $\mathcal{R}(\mathbf{w}_F, \mathbf{w}_S; \alpha_*) = \mathbf{0}$  for  $\mathbf{w}_F$  and  $\mathbf{w}_S$ .
23:        $\mathcal{A} \leftarrow \mathcal{A} \cup \{\alpha_*\}$ 
24:     end if
25:     Evaluate objective function  $c(\mathbf{w}_S, \alpha_*)$  and constraints  $\mathbf{g}(\mathbf{w}_S, \alpha_*), \mathbf{h}(\mathbf{w}_S, \alpha_*)$ .
26:   end for
27:   Check stopping criterion. If satisfied,
28:   break
```

29: **Part 2: Find best design and check stopping criterion**

30: Identify the best design in the current iteration:

31: $\alpha_{\text{opt}} = \arg \min_{\{\alpha_i^{(k)}, i=1, \dots, M\}} \left[c(\mathbf{w}_S, \alpha_i^{(k)}) + \mu \left(\|\max(\mathbf{0}, \mathbf{g}(\mathbf{w}_S, \alpha_i^{(k)}))\|^2 + \|\mathbf{h}(\mathbf{w}_S, \alpha_i^{(k)})\|^2 \right) \right]$

32: **if** $\alpha_{\text{opt}} \notin \mathcal{A}$ **then**

33: Solve coupled FSI problem $\mathcal{R}(\mathbf{w}_F, \mathbf{w}_S; \alpha_{\text{opt}}) = \mathbf{0}$ for \mathbf{w}_F and \mathbf{w}_S .

34: $\mathcal{A} \leftarrow \mathcal{A} \cup \{\alpha_{\text{opt}}\}$

35: Re-evaluate objective function $c(\mathbf{w}_S, \alpha_{\text{opt}})$ and constraints $\mathbf{g}(\mathbf{w}_S, \alpha_{\text{opt}})$, $\mathbf{h}(\mathbf{w}_S, \alpha_{\text{opt}})$.

36: **end if**

37: **Part 3: Update dataset and GPR model**

38: Update $N_{\text{true}} = |\mathcal{A}|$.

39: Reset $\mathcal{D} = \emptyset$.

40: **if** $N_{\text{true}} \geq N_\beta$ **then**

41: **for** $i = 1, \dots, N_{\text{true}}$ **do**

42: Compute $\tilde{p}(\mathbf{X}, t; \alpha_i)$ by (32), using N_b nearest neighbors from $\mathcal{A} \setminus \{\alpha_i\}$.

43: Compute $e_i = e(\alpha_i)$ by (42).

44: $\mathcal{D} \leftarrow \mathcal{D} \cup \{(\alpha_i, e_i)\}$

45: **end for**

46: Assemble vector $\mathbf{e} = [e_1, e_2, \dots, e_{N_{\text{true}}}]^T$ and matrix $\mathbf{Y} = [\mathbf{y}(\alpha_1), \mathbf{y}(\alpha_2), \dots, \mathbf{y}(\alpha_{N_{\text{true}}})]$.

47: Compute $\{\sigma_m^2, \{\theta_j\}_{j=1}^d, \sigma^2\}$ by maximizing log marginal likelihood (55).

48: Assemble covariance matrix $\mathbf{K} \in \mathbb{R}^{N_{\text{true}} \times N_{\text{true}}}$ by (47); compute \mathbf{K}^{-1} by Cholesky factorization.

49: Compute $\bar{\boldsymbol{\beta}}$ by (50).

50: **end if**

51: **Part 4: Update design candidates**

52: Apply a gradient-free update rule to obtain new design candidates $\{\alpha_1^{(k+1)}, \dots, \alpha_M^{(k+1)}\}$.

53: **end for**

Output: Final design: α_{opt}

A few details in Algorithm 2 deserve further clarification. During the first iteration ($k = 1$) and until the number of coupled CFD–CSD analyses is sufficiently large to construct the GPR model (i.e., $N_{\text{true}} \geq N_\beta$), all candidate designs are evaluated using coupled simulations. When Lines 9 and 10 are executed, the GPR model must have been constructed in Part 3 during the previous iteration. In Part 2, if the best design in the current iteration was evaluated using the surrogate model, the algorithm performs an additional coupled simulation at this design point. This step

This new architecture is referred to as SOFICS-AMF, to distinguish it from the baseline SOFICS-Base illustrated in Fig. 5. However, SOFICS-AMF can be viewed as a backward-compatible extension of SOFICS-Base. Setting the decision model tolerances $\tau_u = \tau_e = 0$ reduces the framework to the baseline workflow, in which the surrogate model is never accepted and all design evaluations are performed through coupled analyses.

4.3. Computational cost

While the adaptive decision model introduces the GPR into the workflow, the associated computational overhead is trivial compared to the cost of coupled CFD–CSD analysis.

In the worst-case scenario, the GPR model decides to evaluate all candidate designs using coupled CFD–CSD analyses. The additional overhead incurred comes from three operations: (1) computing the fluid pressure (or traction vector) approximation errors, (2) updating the error dataset \mathcal{D} , and (3) calibrating the GPR model using the updated dataset. Among these, the error computation step is inexpensive, as it only involves evaluating quantities defined on the lower-dimensional fluid-structure interface rather than the full fluid domain Ω_F . Additionally, the nearest-neighbor search required for pressure approximation has a computational complexity of $\mathcal{O}(dN_{\text{true}})$, which remains modest because both the design space dimension d and the number of FSI samples N_{true} are small relative to the size of the full fluid discretization.

The dominant additional cost comes from calibrating the GPR model, which may scale cubically with the size of the regression dataset, i.e., $\mathcal{O}(N_{\text{true}}^3)$. However, this is still trivial compared to the cost of a coupled CFD–CSD analysis. In contrast, the cost of a coupled CFD–CSD analysis is typically on the order of $\mathcal{O}(N^2 \log N)$ for the fluid sub-problem, where N represents the total number of spatial and temporal grid points, and on the order of $\mathcal{O}(n^2 \log n)$ for the structural sub-problem, with $n \ll N$. As a result, unless the size of the GPR training dataset approaches the scale of the fluid discretization—which is rarely the case in practice—the overhead introduced by the adaptive framework remains negligible relative to the cost of solving a FSI problem.

5. Numerical Experiments

5.1. Piston in one-dimensional flow

We consider a one-dimensional FSI problem involving a compressible, inviscid fluid flow interacting with a piston supported by two linear springs. The problem setup is illustrated in Fig. 7(a). The fluid sub-problem, \mathcal{R}_F , is governed by Eqs. (4) and (5), reduced to one spatial dimension. The structural sub-problem, \mathcal{R}_S , is described by

$$\bar{M}\ddot{w}(t) + \bar{D}w(t) = p_F(t)A, \quad w(0) = 0, \quad \dot{w}(0) = 0, \quad (58)$$

where $w(t)$ denotes the piston displacement. \bar{M} and \bar{D} are the structure’s mass and stiffness, given by

$$\bar{M} = M_1 + M_2, \quad \bar{D} = \left(\frac{1}{D_1} + \frac{1}{D_2} \right)^{-1}, \quad (59)$$

with M_i and D_i representing the mass and stiffness of spring i ($i = 1, 2$). Here, $p_F(t)$ denotes the fluid pressure acting on the piston surface, and $A = 1 \text{ mm}^2$ is the piston area.

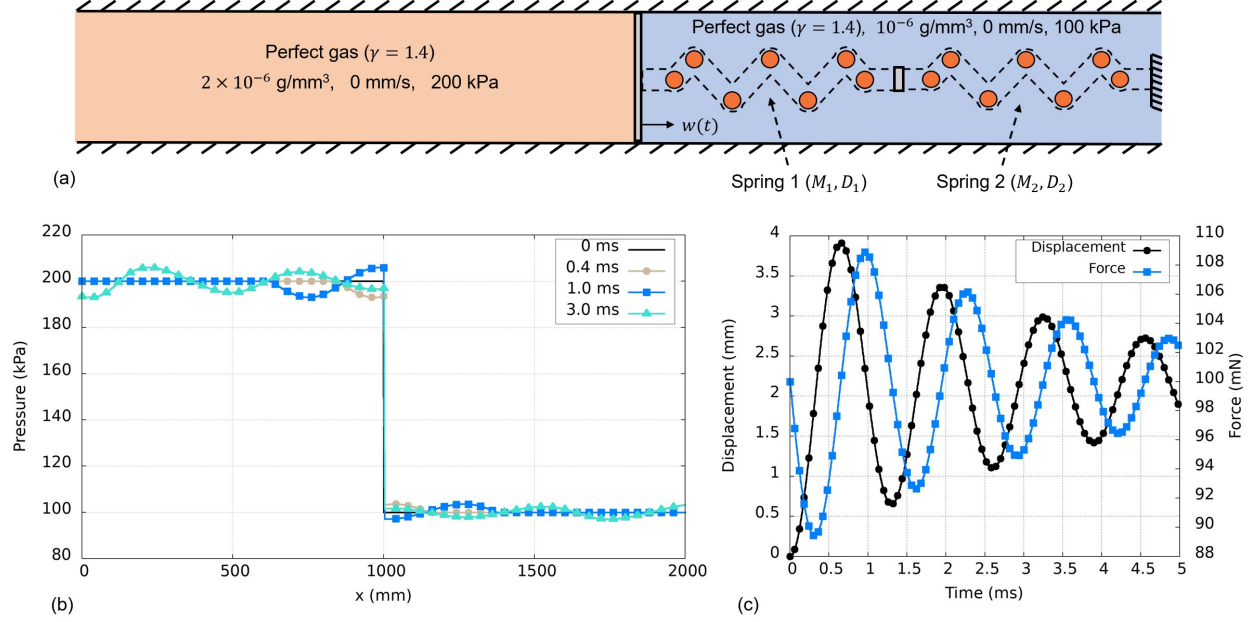


Fig. 7: Piston in a one-dimensional flow. (a) Problem setup. (b) Fluid pressure field for $\alpha_{(1)} = 1.25$ and $\alpha_{(2)} = 0.75$. (c) Time histories of piston displacement and fluid load, $p_F(t)A$, for the same design.

We introduce a two-dimensional design space parameterized by the non-dimensional design variables $\alpha = [\alpha_{(1)}, \alpha_{(2)}]^T$, which controls both the mass and stiffness of each spring. Specifically, for $i = 1, 2$,

$$D_i = c_D \alpha_{(i)}, \quad M_i = c_M \alpha_{(i)}, \quad (60)$$

where $c_D = 10^5 \text{ g/s}^2$ and $c_M = 10^{-3} \text{ g}$.

The optimization problem seeks to minimize the maximum piston velocity, $\|\dot{w}(t)\|_\infty$, subject to inequality constraints on the design variables and piston displacement:

$$\begin{aligned} & \underset{\alpha \in \Omega_D}{\text{minimize}} && \|\dot{w}(t; \alpha)\|_\infty \\ & \text{subject to} && \alpha_{(1)} + \alpha_{(2)} \leq 2.0, \\ & && \alpha_{(1)} - \alpha_{(2)} \geq 0.5, \\ & && w(t; \alpha) \leq 10.0 \text{ mm}, \quad \forall t > 0, \end{aligned} \quad (61)$$

where $\Omega_D = [0.2, 2.0]^2$.

By construction, the optimal solution occurs when the first two constraints hold as equalities, yielding $\alpha_{\text{opt}} = [1.25, 0.75]^T$. This can be understood by noticing that the maximum displacement and velocity both decrease with

increasing mass \bar{M} and stiffness \bar{D} . When $\bar{M} = c_M(\alpha_{(1)} + \alpha_{(2)})$ is fixed, \bar{D} is maximized when $\alpha_{(1)}$ and $\alpha_{(2)}$ are as close as possible.

Figure 7(b) and (c) show the results of the coupled FSI analysis at the optimal design. Initially, a higher fluid pressure on the left side drives the piston to the right. As the piston compresses, the restoring elastic force increases and eventually reverses the motion, pushing the piston back to the left, ultimately leading to an oscillatory motion.

The optimization problem is solved using the two methods described in Sec. 4:

- **BASE**: The baseline framework from Sec. 4.1 (i.e., SOFICS-Base) is employed. Every candidate design is evaluated using a coupled CFD–CSD analysis. The piston surface is represented as an embedded surface in the fluid domain, and the same fluid mesh is used for all designs.
- **AMF**: The adaptive multi-fidelity framework from Sec. 4.2 (i.e., SOFICS-AMF) is used. For each candidate design, the GPR model predicts the surface pressure approximation error and its associated uncertainty. Using the tolerances $\tau_e = 1.3\%$ and $\tau_u = 1\%$, the decision model selects between a coupled CFD–CSD analysis and a structure-only analysis in which transient, distributed fluid pressure loads are computed using surrogate model (32). The pressure is interpolated from $N_b = 5$ nearest neighbors in the design space.

The same genetic algorithm settings are used in both cases. The initial population consists of 20 designs generated randomly within Ω_D . The selection operator is chosen to favor feasible designs. Shuffle-random crossover is used with a crossover rate of 0.1, while offset-normal mutation is used with a mutation rate of 1.0 and a mutation scale of 0.02. In both cases, the optimization is run for 20 iterations.

Figure 8 presents the evolution of the design populations in **BASE**. The two linear inequality constraints active at the optimum are also plotted. Beginning at Iteration 5, the population lies entirely within the feasible region and progressively converges toward the true solution. At the final iteration (Iteration 20), the optimizer provides $\alpha_{\text{opt}}^{(\text{BASE})} = [1.258, 0.736]^T$, which differs from the true optimum by 1.1%.

Figure 9 shows the corresponding results for **AMF**. Similar convergence toward the true optimum is observed throughout the optimization process. At Iteration 20, the final design is $\alpha_{\text{opt}}^{(\text{AMF})} = [1.249, 0.748]^T$, corresponding to an error of only 0.16%. While the convergence trend is expected, the smaller final error relative to **BASE** is likely coincidental.

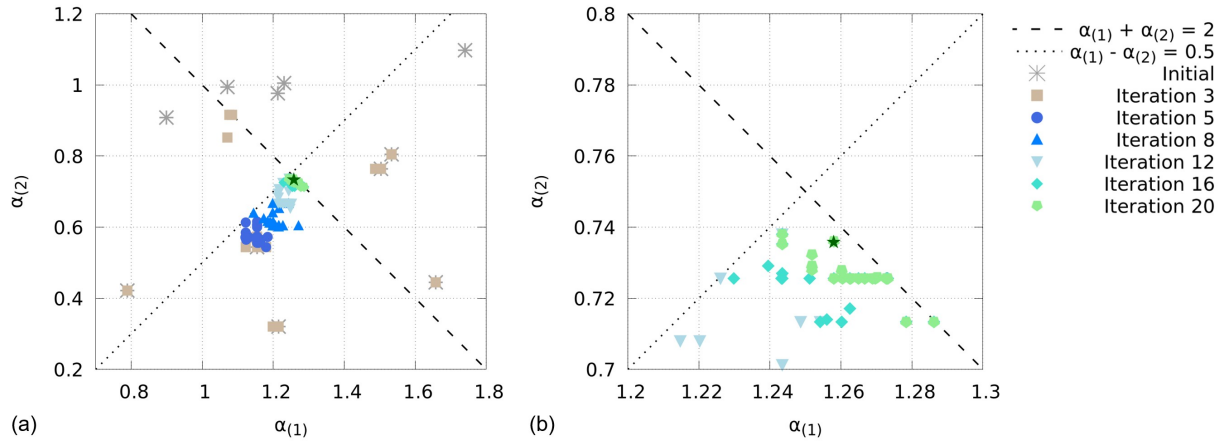


Fig. 8: Evolution of the design populations in **BASE**. (a) Broader view of the design space; (b) detailed view in the vicinity of the optimum. The final design is marked with a pentagram. For reference, the two linear constraints are also shown, and the true optimum lies at their intersection.

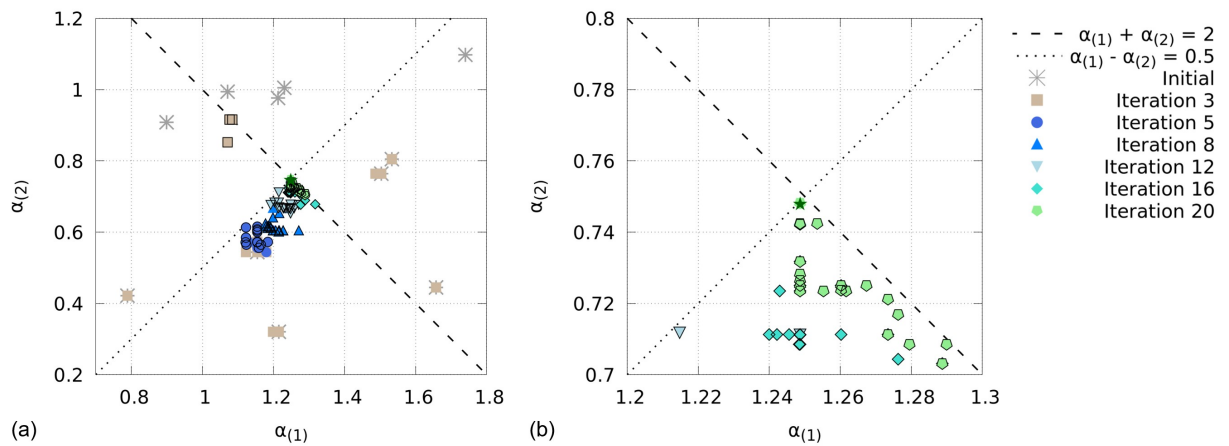


Fig. 9: Evolution of the design populations in **AMF**. (a) Broader view of the design space; (b) detailed view in the vicinity of the optimum. Designs evaluated using the surrogate model are indicated by black outlines, and the final design is marked with a pentagram.

Figure 9 identifies the designs evaluated using the surrogate fluid model with black outlines. Beginning in Iteration 3, three designs are evaluated using the surrogate model. This number increases to 13 in Iteration 5, and from Iteration 6 onward, the vast majority of designs are evaluated in this way. Overall, 347 out of 407 design evaluations (85%) are performed using the surrogate model. By comparison, **BASE** also requires 407 design evaluations, all based on coupled analyses. Since the computational cost of the piston solver is negligible relative to the CFD solver, the overall computational cost reduction is close to 85%.

5.2. Flexible panel under shock loading

5.2.1. Problem description

Next, we demonstrate the proposed adaptive multi-fidelity optimization framework using the two-dimensional model problem illustrated in Fig. 10. The problem involves a slender panel subject to a planar shock wave. When the shock impinges on the panel, it produces a reflected wave traveling upstream, a transmitted shock that diffracts around the panel tip, and vortex structures that interact with reflected waves from the domain boundaries. These nonlinear, transient flow features generate a time-dependent pressure distribution on the panel surface. Meanwhile, the panel is designed to be flexible and bends under the fluid loading.

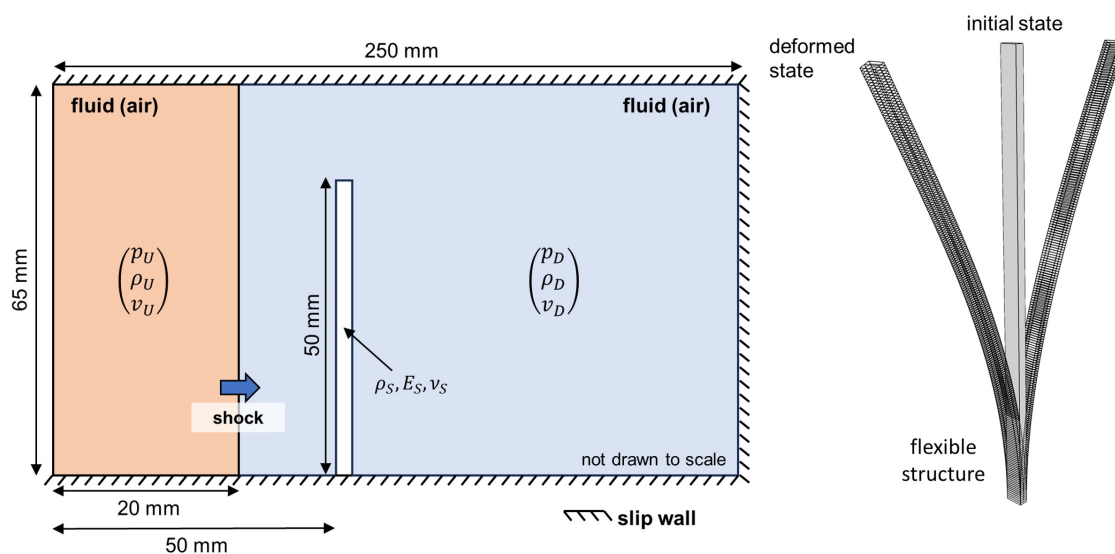


Fig. 10: A flexible cantilever panel subject to shock loading.

This configuration was previously investigated by Giordano *et al.* [53] as a canonical FSI problem relevant to a range of aerospace and defense applications. The geometric and material properties adopted in the present study largely follow their setup. The fluid flow surrounding the panel is modeled as a compressible, inviscid perfect gas governed by the Euler equations (5). The computational domain is a two-dimensional rectangular region of length 250 mm and height 65 mm. A planar shock wave with Mach number 1.21 is initialized 20 mm from the inlet boundary and propagates from left to right. The upstream fluid state is specified as $p_U = 155.7$ kPa, $\rho_U = 1.63$ kg m⁻³, and $v_U = 109.6$ m s⁻¹, while the downstream state corresponds to ambient conditions with $p_D = 101$ kPa, $\rho_D = 1.2$ kg m⁻³, and $v_D = 0$ m s⁻¹. The panel is 50 mm tall and is made of steel, with density $\rho_S = 7600$ kg m⁻³, Young's modulus $E_S = 220$ GPa, and Poisson's ratio $\nu_S = 0.33$. It is clamped at its base, while its other boundaries are free to deform and exposed to the fluid. Fluid-structure coupling is enforced through the kinematic and dynamic interface conditions defined in (6) and (8), respectively.

5.2.2. Validation of coupled CFD–CSD analysis

For a reference panel with a uniform thickness of 1 mm, we compare the results obtained using our simulation framework (i.e., M2C and Aero-S) with the numerical and experimental results from Giordano *et al.* [53]. The fluid domain is discretized by a non-uniform, non-body conforming Cartesian mesh of 57,460 nodes, with a minimum element size of 0.25 mm near the fluid–structure interface. The panel is discretized with 0.5 mm hexahedral elements, resulting in a total of 200 elements. Fig. 11 presents a qualitative comparison of the overall flow field using synthetic Schlieren images (i.e., the magnitude of density gradient) from the present study, together with the numerical Schlieren fields and experimental shadowgraph images extracted from Giordano *et al.* When the incident planar shock reaches the flexible panel, the impact generates a reflected shock traveling upstream and a transmitted shock propagating downstream into the ambient fluid. As reported in the reference study, the transmitted shock subsequently develops into a curved front as the flow area increases behind the panel. As the flow evolves, vortex structures form near the panel tip and are convected downstream, interacting with other nonlinear flow features such as reflected shocks and expansion waves originating from the right wall. These backward-propagating waves eventually impact on the panel again, inducing additional deformation. Overall, the present results show good agreement with both the experimental observations and the numerical results reported in the reference study.

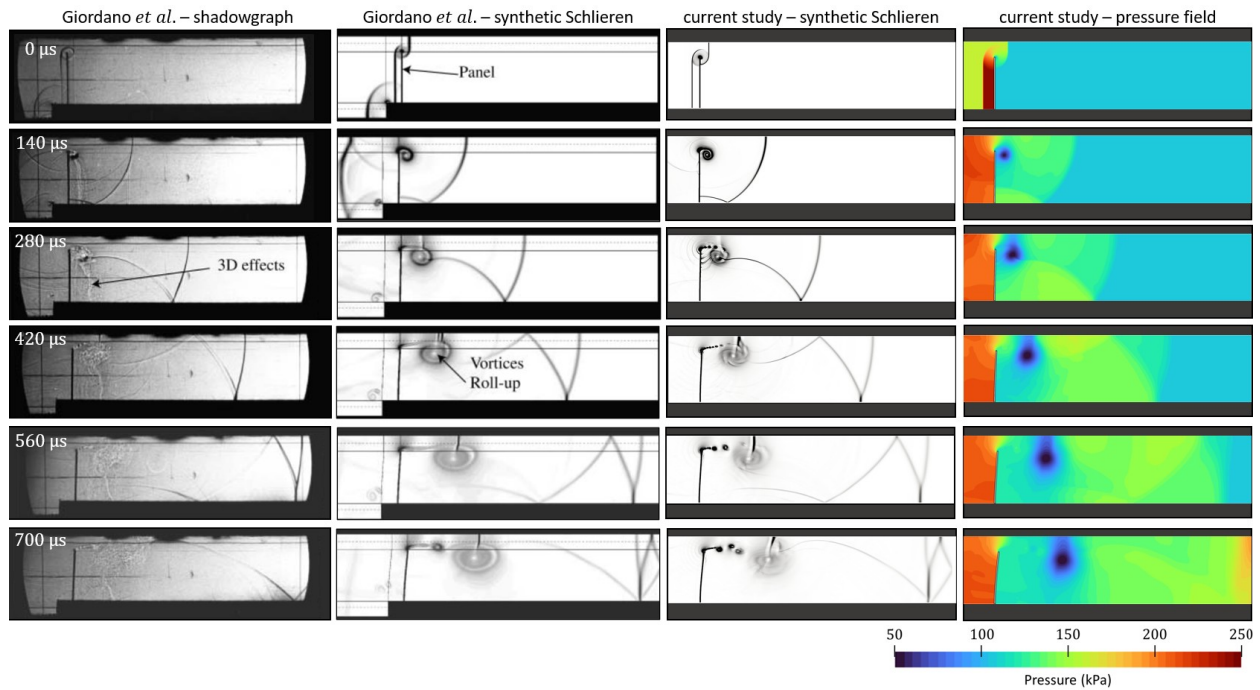


Fig. 11: Comparison of current simulation result with published data for a reference design ($\alpha = [1.0, 1.0, 1.0]^T$).

In addition, quantitative comparison of the panel's tip displacement also shows reasonable agreement. The peak horizontal displacement predicted in the present simulation is 5.76 mm, compared with the experimental measurement

of 6.2 ± 0.4 mm and the numerical result of 6.6 mm reported by Giordano *et al.* Additional details can be found in [54]. It should be noted that the present simulation setup does not include the rigid ramp in the experimental and computational configurations of Giordano *et al.*. This leads to some discrepancies in the result. Moreover, the simulation and experimental data reported in the reference study themselves exhibit noticeable differences, which are discussed in Giordano *et al.* [53].

5.2.3. Design of optimization study

We consider a shape optimization problem in which the panel geometry is modified by varying the thickness at three lengthwise sections. The design variable is defined as $\alpha = [\alpha_{(1)}, \alpha_{(2)}, \alpha_{(3)}]^T$, where $\alpha_{(1)}$, $\alpha_{(2)}$, and $\alpha_{(3)}$ denote the thicknesses (in mm) of the tip, mid-section, and clamped base, respectively. The thickness distribution between these locations is set by linear interpolation.

The optimization objective is to minimize the peak horizontal displacement of the panel's tip, $\|w_x(\mathbf{X}_{\text{tip}}, t)\|_{\infty}$, subject to constraints on the maximum von Mises stress at the clamped base $\sigma_{\text{VM}}(\mathbf{X}_{\text{base}}, t)$ and the total structural mass M . This constrained optimization problem is stated as

$$\begin{aligned} & \underset{\alpha \in \Omega_D}{\text{minimize}} && \|w_x(\mathbf{X}_{\text{tip}}, t; \alpha)\|_{\infty} \\ & \text{subject to} && \sigma_{\text{VM}}(\mathbf{X}_{\text{base}}, t; \alpha) \leq 500 \text{ MPa}, \\ & && M(\alpha) \leq 0.76 \text{ g}, \end{aligned} \tag{62}$$

where $\Omega_D = [0.5, 4.0]^3$ limits the design space to a bounded rectangular region. The constrained problem is converted to an unconstrained one through an exterior penalty method, with the structural response normalized by reference values $w^{\text{ref}} = 6.0$ mm, $\sigma^{\text{ref}} = 800$ MPa, and $M^{\text{ref}} = 0.76$ g.

In this problem, the fluid domain is substantially larger than the structural domain, meaning that the computational cost of each coupled analysis is dominated by the CFD solver. The objective and constraints are common in structural design optimization, and the trade-offs between stiffness and weight can be rationalized from elementary beam theory.

To evaluate the proposed framework, three optimization studies are conducted, differing only in how the fluid subproblem is treated.

- **BASE:** The baseline optimization framework described in Sec. 4.1 (i.e., SOFICS-Base) is employed. Because the CFD solver employs an embedded boundary method, the fluid mesh remains unchanged for all designs; only the structural mesh is updated.
- **AMF:** The adaptive multi-fidelity framework described in Sec. 4.2 (i.e., SOFICS-AMF) is employed. $\tau_e = 1.3\%$, $\tau_u = 1\%$, and $N_b = 5$.
- **DRY:** Every design is evaluated by solving only the structural sub-problem \mathcal{R}_S . The fluid-induced loads are prescribed using the pressure time-history obtained from the coupled CFD-CSD analysis of the reference panel

(i.e., $\alpha = [1.0, 1.0, 1.0]^T$). This study can be viewed as a limiting case of **AMF** under large tolerances τ_e and τ_u . It also reflects the conventional structural optimization approach, in which external loads are specified *a priori*.

The design space is explored using a single-objective genetic algorithm. Table 1 summarizes the main algorithmic settings and parameter values, most of which are default options in Dakota. The initial population is generated by Latin Hypercube Sampling (LHS) within the subdomain $[2.5, 4.0]^3$ of the design space. This choice is deliberate. Panels in this region are uniformly thick, and therefore heavy and stiff. While the tip displacement is small and the stress constraint is easily satisfied, the mass constraint is violated, resulting in a high penalized merit function value for every initial design. The optimizer is thus forced to explore the design space incrementally towards the feasible region, thereby testing the surrogate model’s adaptability as the evaluated designs shift progressively away from the initial cluster. Furthermore, the optimal design is expected to feature a tapered profile (i.e., $\alpha_{(1)} < \alpha_{(2)} < \alpha_{(3)}$), which lies far from the initial population. Starting from a distant, uniformly thick region therefore also demonstrates the ability of the genetic algorithm to locate the global minimum without being trapped in a local minimum.

Table 1: Summary of Dakota input parameters used in the optimization study.

Item	Inputs
Seed	1649919949
Initial population	Size: 50 Type: user-specified (randomly distributed within $[2.5, 4]^3$)
Fitness	Type: exterior-penalty merit function Constraint penalty parameter: 20.0
Crossover	Type: shuffle random Number of parents: 2 Number of offspring: 2 Crossover rate: 0.8
Mutation	Type: replace-uniform mutation Mutation rate: 0.3
Replacement	Type: elitist
Stop criterion	Maximum number of iterations: 30

5.2.4. Results and discussion

In all three cases, the optimizer was run for 30 iterations. As shown in Fig. 12(a), the merit function value starts at approximately 55 in each case. By the end of the optimization, all the three cases have yielded significant reduction in the merit function value. The value decreases to 0.45 for **BASE** and **AMF**, and to 0.92 for **DRY**. Fig. 12(b) shows

the evolution of the optimal design throughout the optimization process. Taking the final result from **BASE** as the reference, the error in the **AMF** result is 2.3%, compared with 17.0% for **DRY**.

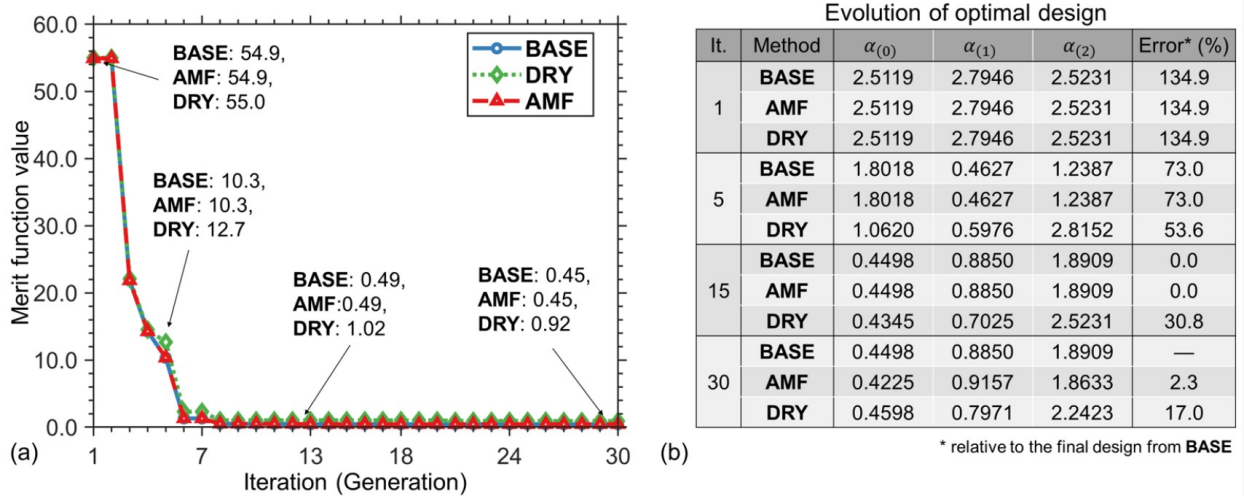


Fig. 12: Comparison of the three methods **BASE**, **AMF**, and **DRY**. (a) Iteration history of the merit function; (b) evolution of the optimal design at four iterations. The error in α is calculated using the final result from **BASE** as reference.

Figure 13 illustrates the evolution of the design population over successive iterations in **BASE**. The genetic algorithm (GA) initially focuses on exploring the design space, gradually shifting the population away from the initial samples with high panel thicknesses. By iteration 4, the population begins to move toward lower-thickness regions, with a noticeable preference for designs in which $\alpha_{(2)}$ is relatively small, as reflected by the best design in that iteration. Continued exploration guides the GA toward a region containing tapered panel geometries around iteration 12. This transition is also reflected in the merit function history shown in Fig. 12, where the objective value improves by approximately one order of magnitude relative to the initial population. By iteration 25, the population becomes tightly clustered, and the optimizer converges to an optimal design with thickness parameters $\alpha_{\text{opt}}^{(\text{BASE})} = [0.44, 0.88, 1.89]^T$ mm. The resulting configuration exhibits a pronounced taper from tip to base, consistent with the physical expectation that the required structural stiffness increases toward the clamped support, where bending moments are largest.

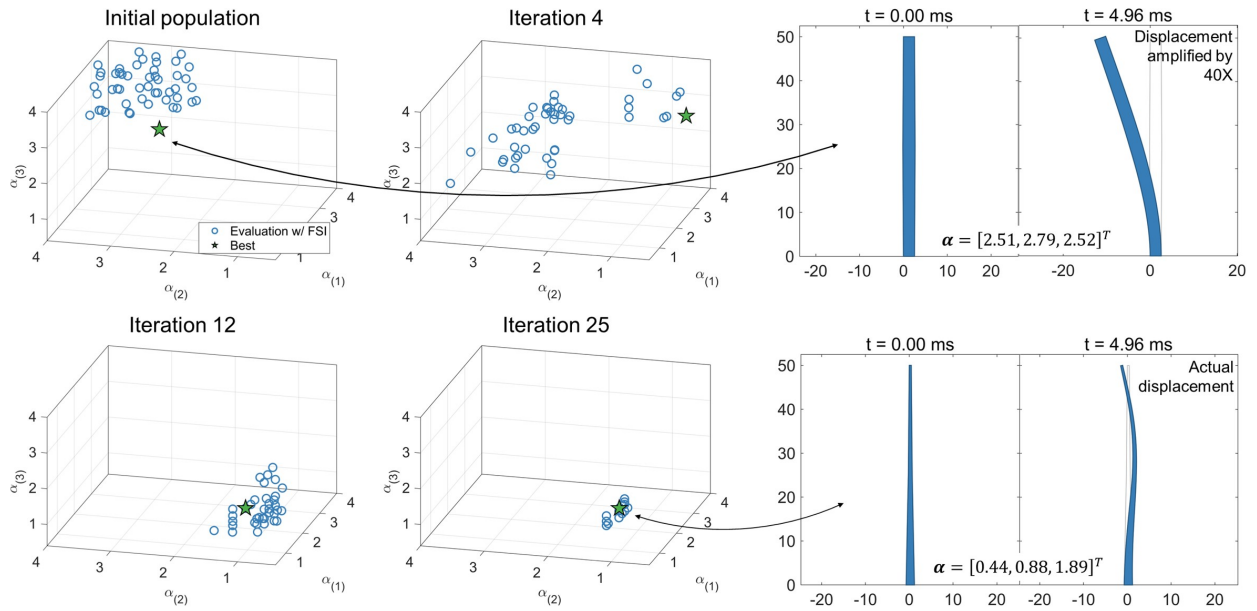


Fig. 13: Design population at selected iterations of the **BASE** optimization study. Scatter plots show candidate designs in the three-dimensional design space, with the current best design marked by a pentagram.

The convergence behavior observed from **BASE** provides a rationale for the proposed adaptive multi-fidelity framework. Figure 14 shows the pressure time history at the panel tip. The result corresponding to the optimal design $\alpha_{\text{opt}}^{(\text{BASE})}$ is shown as a thick solid line. Three iterations—1, 15, and 30—are selected for comparison. For each iteration, the five nearest neighbors of $\alpha_{\text{opt}}^{(\text{BASE})}$ among the evaluated designs up to that iteration are identified, representing the designs that would be used for interpolating the fluid-induced load at $\alpha_{\text{opt}}^{(\text{BASE})}$ in the surrogate model. The pressure histories associated with these neighboring designs are plotted in different colors.

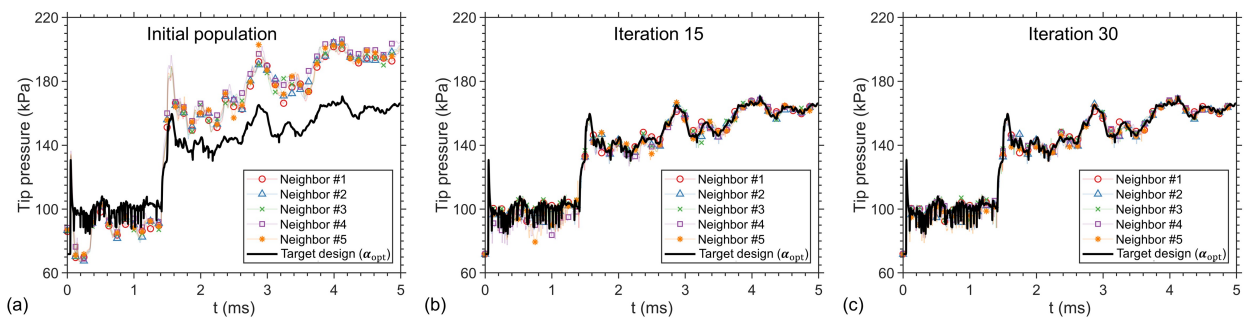


Fig. 14: Pressure time histories recorded at the panel's tip across selected iterations of the **BASE** optimization study.

In the initial population, the sampled designs lie far from $\alpha_{\text{opt}}^{(\text{BASE})}$ (see Fig. 13), and the pressure histories at the five neighbors deviate substantially from that of $\alpha_{\text{opt}}^{(\text{BASE})}$. This reflects the FSI in the problem: the pressure loading on the structure varies with the structural design variables. It also implies the necessity of a decision model that limits the

use of surrogate evaluations in such situations, reverting to coupled CFD–CSD analyses until sufficient local data have been accumulated. In later iterations (e.g., 15 and 30), as the population concentrates within a small neighborhood of the optimal design, the pressure histories associated with neighboring designs converge toward a common profile. As a result, the accuracy of the interpolation surrogate model improves. The GPR-based decision model is expected to track this evolving accuracy and progressively increase the use of surrogate evaluations throughout the optimization.

Figure 15 presents the results obtained from **AMF** at the same iterations as shown in Fig. 13. Design candidates evaluated with the surrogate model are shown in red color. The adaptive multi-fidelity framework reproduces the convergence behavior of **BASE** while substantially reducing the number of coupled CFD–CSD analyses. In the initial iteration, all 50 candidate designs are evaluated using the coupled FSI solver. This number decreases to 8 in iteration 4, 12 in iteration 12, and 1 in iteration 25.

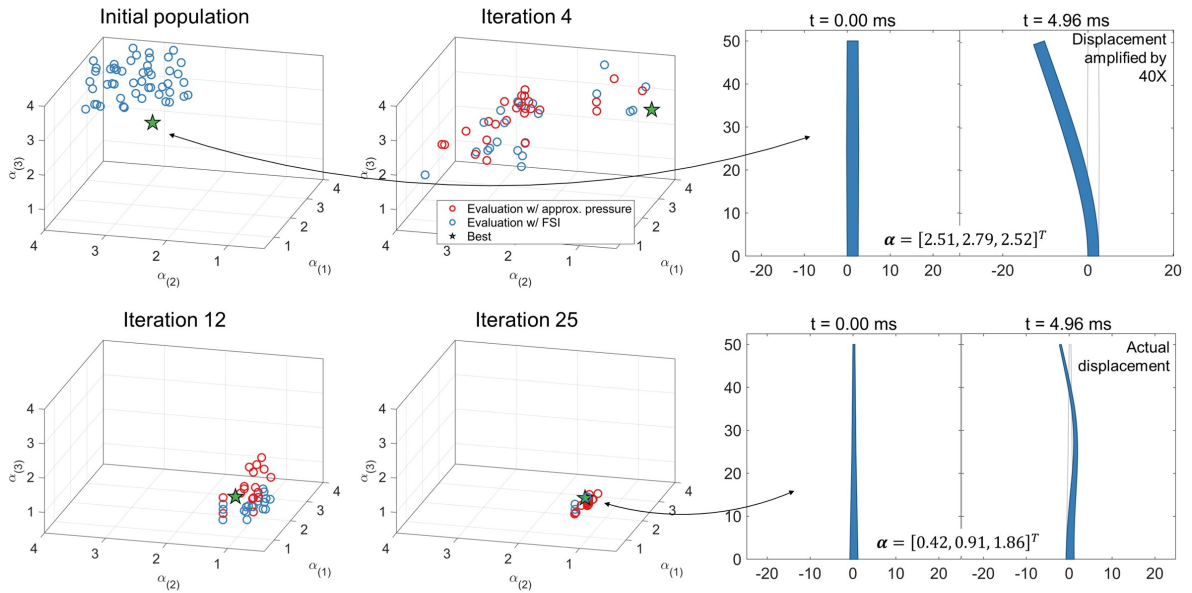


Fig. 15: Evolution of the design population in the **AMF** optimization study. Blue and red circles indicate design candidates evaluated using coupled simulation and surrogate fluid model, respectively. The best design in each iteration is marked by a pentagram.

The number of surrogate-accepted designs is influenced by the crossover and mutation operators and their prescribed rates (Table 1). With a crossover rate of 0.8, most new design points inherit combinations of variables from two parent designs. As a result, they tend to remain within the convex hull of the current population, where the GPR model has already accumulated data and its predictive uncertainty is low. The mutation operator is applied with a rate of 0.3. It generates new designs by replacing one or more variables with values drawn uniformly from the feasible range. Consequently, some designs are placed in unexplored regions of the design space. In these regions, the GPR uncertainty is more likely to exceed the prescribed threshold τ_u , triggering the use of coupled CFD–CSD analysis. As a result, even in later iterations when surrogate-based evaluations dominate, a small but consistent number of designs

still require coupled analysis. These cases typically correspond to mutated offspring that explore sparsely sampled regions of the design space.

The final design obtained from **AMF** is $\alpha_{\text{opt}}^{(\text{AMF})} = [0.42, 0.91, 1.86]^T$. It differs from the result of **BASE** by only 2.3%. Fig. 16 compares the dynamic responses of these two designs in coupled CFD-CSD analyses. The designs show very close agreement, both in geometry and in their transient responses during the FSI process. In contrast, the result obtained from **DRY** is $\alpha_{\text{opt}}^{(\text{DRY})} = [0.46, 0.80, 2.24]^T$, which differs from the **BASE** result by 17.0%.

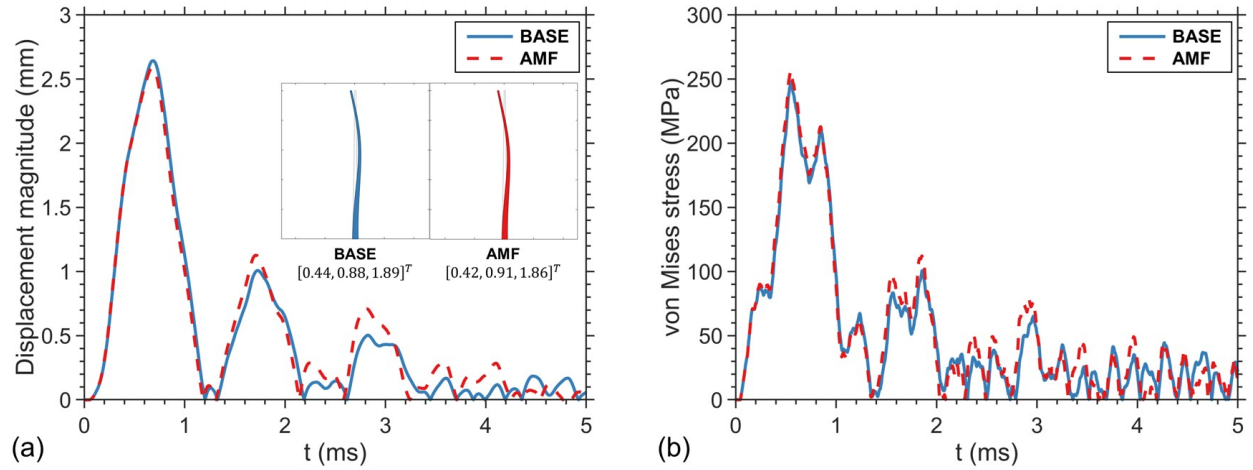


Fig. 16: Comparison of the dynamic responses of the optimal designs obtained from **BASE** and **AMF**. (a) Time history of the panel's tip displacement, and (b) time history of the von Mises stress at the panel's clamped base.

Comparing Figs. 13 and 15, it is notable that **AMF** matches **BASE** not only in the final design but also in the evolution of the population during the optimization process. At each iteration, many designs in the current population closely correspond between the two runs. This suggests that from the optimizer's perspective, **AMF** and **BASE** are largely interchangeable. Meanwhile, the discrepancy between **DRY** and **BASE** is reasonable. Because the fluid-induced loads are pre-specified and fixed across all designs, **DRY** essentially solves a different optimization problem.

Next, we examine the performance of the GPR model for surrogate error estimation. Figure 17 presents the predicted mean error and associated uncertainty at 21 points in the rectangular design space, including eight points near the corners, eight points along the boundary of the mid-surface in $\alpha_{(3)}$, and five interior points corresponding to the optimal designs obtained in five iterations. Predictions based on data accumulated up to iterations 1, 4, 12, and 25 are shown separately. The results indicate that both the predicted error and uncertainty are generally smaller at sample locations lying within clusters of available data. Accordingly, as the iterative process advances and additional samples are collected, the overall prediction error and uncertainty decrease. It is noteworthy that error and uncertainty are not always proportional to each other. There are points in the design space, particularly during the early iterations, where the predicted error is small, yet the associated uncertainty is large. This observation supports the use of both error and uncertainty in the decision model. Moreover, even toward the end of the optimization, some points far from the

optimal design still exhibit relatively large surrogate errors. This behavior reflects a deliberate aspect of our adaptive strategy: the goal is not to construct a globally accurate surrogate across the entire design space, which is unnecessary, but rather to ensure sufficient accuracy in regions where the optimizer explores.

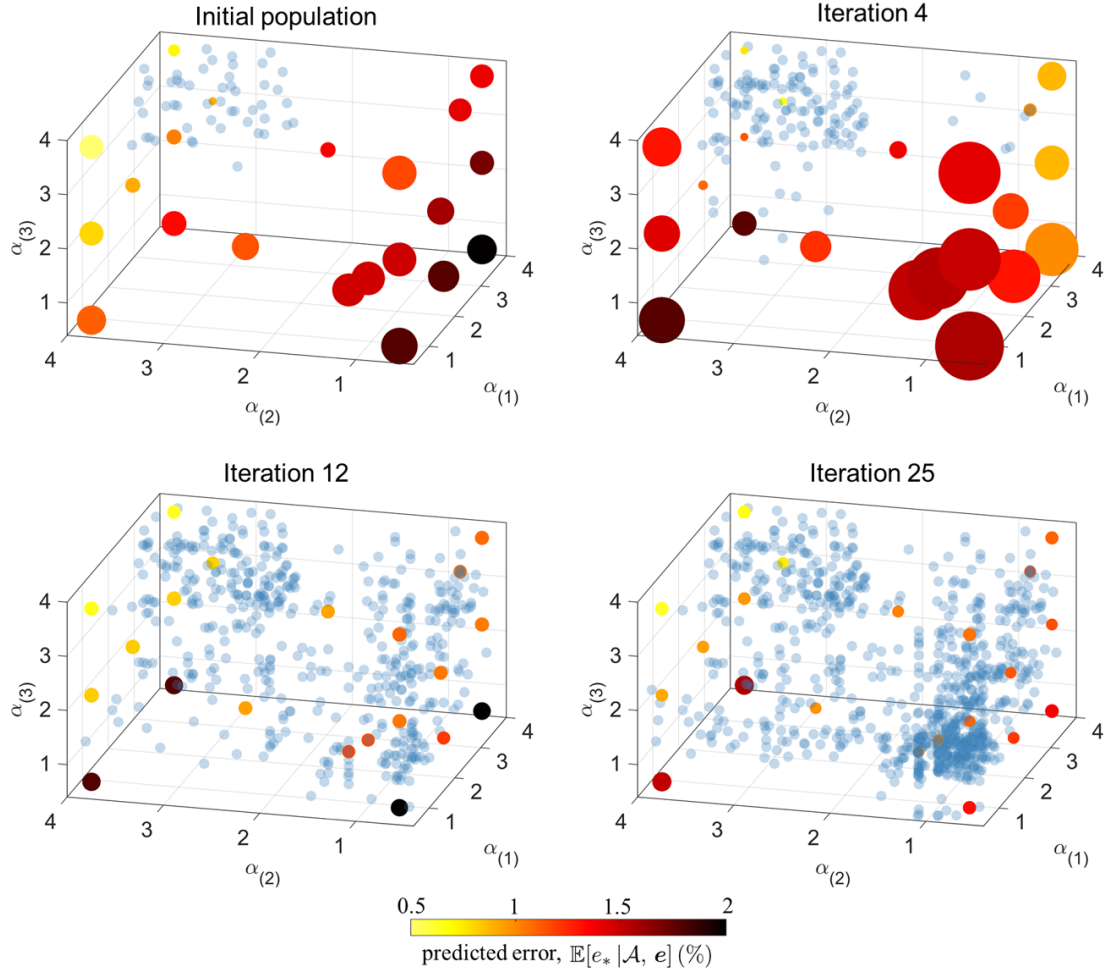


Fig. 17: Surrogate error and uncertainty at 21 points in the design space as estimated by the GPR model, based on CFD-CSD simulation data accumulated up to Iterations 1, 4, 12, and 25. A filled circle is plotted at each point, with color and size representing the mean error $\mathbb{E}[e_* | \mathcal{A}, e]$ and the associated uncertainty u_* , respectively. For reference, the available data points (i.e., \mathcal{A}) used for both the surrogate model and the GPR model are shown as transparent blue circles.

Lastly, we compare the computational cost of the three studies. As shown in Fig. 18, **BASE** required 992 coupled CFD-CSD analyses, resulting in a total cost of approximately 8.8×10^4 CPU core-hours (on the TinkerCliffs computing cluster at Virginia Tech; same below). In comparison, **AMF** reduced both the number of coupled analyses and the total computational cost by about 80%, to 196 analyses and 1.7×10^4 core-hours, respectively. Although an additional 766 CSD simulations using the surrogate fluid-load model were performed, their cost was negligible relative to the coupled analyses. **DRY**, by contrast, required 982 CSD simulations and was indeed computationally inexpensive,

with a total cost of only 364.9 core-hours. However, it produced a design with a substantially larger discrepancy (17.0%).

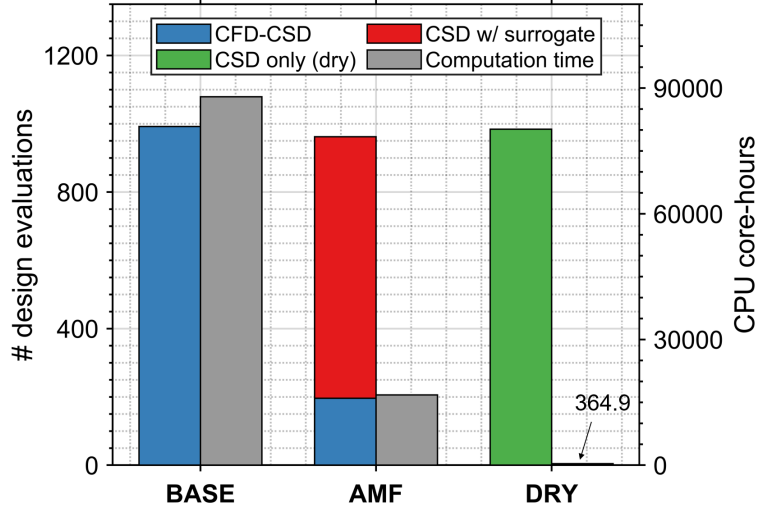


Fig. 18: Cost comparison for the three studies **BASE**, **DRY**, and **AMF**. The number of design evaluations is shown on the left axis; the total computation time is shown on the right axis.

6. Concluding remarks

New high-fidelity analysis capabilities do not directly translate into new design optimization capabilities, as their computational cost is often too high for many-query applications. This is presently the case for structures and vehicles operating under FSI. In practice, designers can often afford optimization based on CSD analyses alone, but not the sharp, orders-of-magnitude increase in cost associated with coupled CFD–CSD analyses.

In this paper, we have presented an adaptive multi-fidelity optimization framework tailored to such problems. The framework builds on recent progress in CFD–CSD coupling, interface tracking, and improved automation of mesh generation. It retains high-fidelity CSD analysis throughout the optimization process. For the computation of fluid-induced loads, it alternates between CFD and a data-driven surrogate, with the choice guided by a GPR model that estimates surrogate error together with uncertainty. The framework does not require any pre-computation such as dataset generation or model training. It is compatible, through parameter adjustments, with both more expensive optimization strategies that rely entirely on coupled analysis and inexpensive structure-only optimization using a fixed load time history. Although not explored directly in this paper, previously available coupled analysis data can be incorporated into the framework by initializing \mathcal{D} and \mathcal{A} with those data at the start of the algorithm.

This adaptive multi-fidelity framework addresses the fundamental trade-off between computational cost and predictive accuracy in design optimization. In this work, we have supported the proposed approach both theoretically, using a simplified FSI model (Sec. 2.3), and numerically through two benchmark problems (Sec. 5). In particular, the

flexible panel under shock loading case demonstrates that the adaptive strategy reduces computational cost by 80%, while introducing only a 2.3% error in the final design.

The proposed framework is modular in nature, allowing straightforward extension to alternative fluid and structural models, solvers, surrogate models, and decision-making strategies. The present study assumes that the optimization objective and constraints do not explicitly depend on the fluid state variables. A natural next step is to relax this assumption and extend the formulation accordingly. Another promising direction is to develop a gradient-based version of the framework to enable more efficient large-scale optimization.

Acknowledgments

The authors gratefully acknowledge support from the Office of Naval Research (ONR) under Award Nos. N00014-23-1-2447 and N00014-24-1-2509; the Naval Air Warfare Center Aircraft Division under Contract No. N6833525C0444; the National Institutes of Health (NIH) under Award Nos. 2R01-DK052985-26 and R01-DK138972; and a research contract from DynaSafe US LLC to Virginia Tech.

References

- [1] M. Motley, Z. Liu, Y. Young, Utilizing fluid–structure interactions to improve energy efficiency of composite marine propellers in spatially varying wake, *Composite structures* 90 (3) (2009) 304–313.
- [2] D.-H. Kim, O.-K. Lim, E.-H. Choi, Y. Noh, Optimization of 5-mw wind turbine blade using fluid structure interaction analysis, *Journal of Mechanical Science and Technology* 31 (2) (2017) 725–732.
- [3] R. Kano, K. Ryuzono, S. Date, Y. Abe, T. Okabe, Structural optimization of composite aircraft wing considering fluid–structure interaction and damage tolerance assessment using continuum damage mechanics, *Aerospace Science and Technology* (2025) 110652.
- [4] H. Chung, S. Cao, M. Philen, P. S. Beran, K. G. Wang, Cfd-csd coupled analysis of underwater propulsion using a biomimetic fin-and-joint system, *Computers & Fluids* 172 (2018) 54–66.
- [5] A. L. Marsden, Optimization in cardiovascular modeling, *Annual review of fluid mechanics* 46 (1) (2014) 519–546.
- [6] C. Long, A. Marsden, Y. Bazilevs, Shape optimization of pulsatile ventricular assist devices using fsi to minimize thrombotic risk, *Computational Mechanics* 54 (4) (2014) 921–932.
- [7] W. Ma, X. Zhao, C. Gilbert, K. Wang, Computational analysis of bubble–structure interactions in near-field underwater explosion, *International Journal of Solids and Structures* 242 (2022) 111527.

- [8] A. Narkhede, S. Islam, X. Sun, K. Wang, Fluid–structure coupled simulation framework for lightweight explosion containment structures under large deformations, *International Journal of Impact Engineering* (2025) 105238doi:10.1016/j.ijimpeng.2025.105238.
- [9] K. Kamrin, C. H. Rycroft, J.-C. Nave, Reference map technique for finite-strain elasticity and fluid–solid interaction, *Journal of the Mechanics and Physics of Solids* 60 (11) (2012) 1952–1969.
- [10] M.-L. Cerquaglia, D. Thomas, R. Boman, V. Terrapon, J.-P. Ponthot, A fully partitioned lagrangian framework for fsi problems characterized by free surfaces, large solid deformations and displacements, and strong added-mass effects, *Computer Methods in Applied Mechanics and Engineering* 348 (2019) 409–442.
- [11] K. Wang, A. Rallu, J.-F. Gerbeau, C. Farhat, Algorithms for interface treatment and load computation in embedded boundary methods for fluid and fluid–structure interaction problems, *International Journal for Numerical Methods in Fluids* 67 (9) (2011) 1175–1206. arXiv:https://onlinelibrary.wiley.com/doi/pdf/10.1002/flid.2556, doi:https://doi.org/10.1002/flid.2556.
URL <https://onlinelibrary.wiley.com/doi/abs/10.1002/flid.2556>
- [12] D. Kamensky, M.-C. Hsu, D. Schillinger, J. A. Evans, A. Aggarwal, Y. Bazilevs, M. S. Sacks, T. J. Hughes, An immersogeometric variational framework for fluid–structure interaction: Application to bioprosthetic heart valves, *Computer methods in applied mechanics and engineering* 284 (2015) 1005–1053.
- [13] S. Cao, A. Main, K. G. Wang, Robin-neumann transmission conditions for fluid-structure coupling: embedded boundary implementation and parameter analysis, *International Journal for Numerical Methods in Engineering* 115 (5) (2018) 578–603.
- [14] J. A. González, K. Park, Three-field partitioned analysis of fluid–structure interaction problems with a consistent interface model, *Computer Methods in Applied Mechanics and Engineering* 414 (2023) 116134.
- [15] B. A. Miller, J. J. McNamara, Efficient fluid-thermal-structural time marching with computational fluid dynamics, *AIAA Journal* 56 (9) (2018) 3610–3621.
- [16] M.-P. Errera, F. Duchaine, Comparative study of coupling coefficients in dirichlet–robin procedure for fluid–structure aerothermal simulations, *Journal of Computational Physics* 312 (2016) 218–234.
- [17] V. Gravemeier, S. M. Civaner, W. A. Wall, A partitioned-monolithic finite element method for thermo-fluid–structure interaction, *Computer Methods in Applied Mechanics and Engineering* 401 (2022) 115596.
- [18] N. V. Queipo, R. T. Haftka, W. Shyy, T. Goel, R. Vaidyanathan, P. K. Tucker, Surrogate-based analysis and optimization, *Progress in aerospace sciences* 41 (1) (2005) 1–28.

- [19] B. Liu, Q. Zhang, G. G. Gielen, A gaussian process surrogate model assisted evolutionary algorithm for medium scale expensive optimization problems, *IEEE Transactions on Evolutionary Computation* 18 (2) (2013) 180–192.
- [20] Y. Zhang, S. Hu, Y. Zhang, L. Chen, Optimization and analysis of centrifugal pump considering fluid-structure interaction, *The scientific world journal* 2014 (1) (2014) 131802.
- [21] M. Yoshimura, K. Shimoyama, T. Misaka, S. Obayashi, Topology optimization of fluid problems using genetic algorithm assisted by the kriging model, *International Journal for Numerical Methods in Engineering* 109 (4) (2017) 514–532.
- [22] M. C. Wu, D. Kamensky, C. Wang, A. J. Herrema, F. Xu, M. S. Pigazzini, A. Verma, A. L. Marsden, Y. Bazilevs, M.-C. Hsu, Optimizing fluid–structure interaction systems with immersogeometric analysis and surrogate modeling: Application to a hydraulic arresting gear, *Computer Methods in Applied Mechanics and Engineering* 316 (2017) 668–693.
- [23] A. F. Ribeiro, D. Casalino, C. Ferreira, Free wake panel method simulations of a highly flexible wing in flutter and gusts, *Journal of Fluids and Structures* 121 (2023) 103955.
- [24] E. Ortega, R. Flores, E. Cuartero, E. Oñate, Efficient aeroelastic analysis of inflatable structures using enhanced potential flow aerodynamics, *Journal of Fluids and Structures* 90 (2019) 230–245.
- [25] L. Ma, Y. Hu, J. Zheng, G. Deng, Y. Chen, Failure analysis for cylindrical explosion containment vessels, *Engineering Failure Analysis* 17 (5) (2010) 1221–1229.
- [26] M. J. Zahr, C. Farhat, Progressive construction of a parametric reduced-order model for pde-constrained optimization, *International Journal for Numerical Methods in Engineering* 102 (5) (2015) 1111–1135.
- [27] R. Tezaur, F. As’ad, C. Farhat, Robust and globally efficient reduction of parametric, highly nonlinear computational models and real time online performance, *Computer Methods in Applied Mechanics and Engineering* 399 (2022) 115392.
- [28] T. Lieu, C. Farhat, M. Lesoinne, Reduced-order fluid/structure modeling of a complete aircraft configuration, *Computer Methods in Applied Mechanics and Engineering* 195 (41) (2006) 5730–5742, John H. Argyris Memorial Issue. Part II. doi:<https://doi.org/10.1016/j.cma.2005.08.026>.
URL <https://www.sciencedirect.com/science/article/pii/S0045782505005153>
- [29] D. Xiao, P. Yang, F. Fang, J. Xiang, C. C. Pain, I. M. Navon, Non-intrusive reduced order modelling of fluid–structure interactions, *Computer Methods in Applied Mechanics and Engineering* 303 (2016) 35–54.
- [30] X. Guo, W. Li, F. Iorio, Convolutional neural networks for steady flow approximation, in: *Proceedings of the 22nd ACM SIGKDD international conference on knowledge discovery and data mining*, 2016, pp. 481–490.

- [31] T. Murata, K. Fukami, K. Fukagata, Nonlinear mode decomposition with convolutional neural networks for fluid dynamics, *Journal of Fluid Mechanics* 882 (2020) A13.
- [32] O. Obiols-Sales, A. Vishnu, N. Malaya, A. Chandramowlishwaran, Cfdnet: A deep learning-based accelerator for fluid simulations, in: *Proceedings of the 34th ACM international conference on supercomputing*, 2020, pp. 1–12.
- [33] D. Kochkov, J. A. Smith, A. Alieva, Q. Wang, M. P. Brenner, S. Hoyer, Machine learning–accelerated computational fluid dynamics, *Proceedings of the National Academy of Sciences* 118 (21) (2021) e2101784118.
- [34] M. Raissi, P. Perdikaris, G. E. Karniadakis, Physics-informed neural networks: A deep learning framework for solving forward and inverse problems involving nonlinear partial differential equations, *Journal of Computational physics* 378 (2019) 686–707.
- [35] X. Fan, J.-X. Wang, Differentiable hybrid neural modeling for fluid-structure interaction, *Journal of Computational Physics* 496 (2024) 112584.
- [36] P. Benner, S. Gugercin, K. Willcox, A survey of projection-based model reduction methods for parametric dynamical systems, *SIAM review* 57 (4) (2015) 483–531.
- [37] M. A. Bouhlel, S. He, J. R. Martins, Scalable gradient–enhanced artificial neural networks for airfoil shape design in the subsonic and transonic regimes, *Structural and Multidisciplinary Optimization* 61 (4) (2020) 1363–1376.
- [38] Y. S. Ong, P. B. Nair, A. J. Keane, Evolutionary optimization of computationally expensive problems via surrogate modeling, *AIAA journal* 41 (4) (2003) 687–696.
- [39] S. Jeong, M. Murayama, K. Yamamoto, Efficient optimization design method using kriging model, *Journal of aircraft* 42 (2) (2005) 413–420.
- [40] R. B. Gramacy, H. K. Lee, Adaptive design and analysis of supercomputer experiments, *Technometrics* 51 (2) (2009) 130–145.
- [41] R. Sanchez, T. Albring, R. Palacios, N. R. Gauger, T. D. Economou, J. J. Alonso, Coupled adjoint-based sensitivities in large-displacement fluid-structure interaction using algorithmic differentiation, *International Journal for Numerical Methods in Engineering* 113 (7) (2018) 1081–1107.
- [42] J. Hron, S. Turek, A monolithic fem/multigrid solver for an ale formulation of fluid-structure interaction with applications in biomechanics, in: *Fluid-Structure Interaction: Modelling, Simulation, Optimisation*, Springer, 2006, pp. 146–170.

- [43] O. Colomés, F. Verdugo, I. Akkerman, A monolithic finite element formulation for the hydroelastic analysis of very large floating structures, *International Journal for Numerical Methods in Engineering* 124 (3) (2023) 714–751.
- [44] C. A. Felippa, K.-C. Park, C. Farhat, Partitioned analysis of coupled mechanical systems, *Computer methods in applied mechanics and engineering* 190 (24-25) (2001) 3247–3270.
- [45] C. Farhat, A. Rallu, K. Wang, T. Belytschko, Robust and provably second-order explicit-explicit and implicit-explicit staggered time-integrators for highly non-linear compressible fluid-structure interaction problems, *International Journal for Numerical Methods in Engineering* 84 (1) (2010) 73–107. doi:10.1002/nme.2883.
- [46] X. Zhao, W. Ma, S. Islam, A. Narkhede, K. Wang, M2c: An open-source software for multiphysics simulation of compressible multi-material flows and fluid-structure interactions, *Computer Physics Communications* 321 (2026) 110023. doi:10.1016/j.cpc.2026.110023.
URL <https://doi.org>
- [47] AeroS (2024). [link].
URL <https://github.com/anarkh97/aero-s-foam>
- [48] M. P. Païdoussis, *Fluid-Structure Interactions: Slender Structures and Axial Flow, Volume 1, 2nd Edition*, Academic Press / Elsevier, Amsterdam; Boston; Heidelberg; London; New York; Oxford, 2013, second edition, revised and updated.
- [49] C. K. Williams, C. E. Rasmussen, *Gaussian processes for machine learning, Vol. 2*, MIT press Cambridge, MA, 2006.
- [50] B. M. Adams, W. J. Bohnhoff, K. R. Dalbey, M. S. Ebeida, J. P. Eddy, M. S. Eldred, R. W. Hooper, P. D. Hough, K. T. Hu, J. D. Jakeman, et al., *Dakota, a multilevel parallel object-oriented framework for design optimization, parameter estimation, uncertainty quantification, and sensitivity analysis: Version 6.16 user’s manual*, Tech. rep., Sandia National Lab.(SNL-NM), Albuquerque, NM (United States) (2022). doi:10.2172/1868142.
URL <https://doi.org/10.2172/1868142>
- [51] A. Main, X. Zeng, P. Avery, C. Farhat, An enhanced FIVER method for multi-material flow problems with second-order convergence rate, *Journal of Computational Physics* 329 (2017) 141–172. doi:10.1016/j.jcp.2016.10.028.
- [52] C. Geuzaine, J.-F. Remacle, Gmsh: A 3-d finite element mesh generator with built-in pre-and post-processing facilities, *International journal for numerical methods in engineering* 79 (11) (2009) 1309–1331.
- [53] J. Giordano, G. Jourdan, Y. Burtschell, M. Medale, D. Zeitoun, L. Houas, Shock wave impacts on deforming panel, an application of fluid-structure interaction, *Shock Waves* 14 (1) (2005) 103–110.

- [54] A. Narkhede, N. Eilers, E. Rivas, K. Wang, Multi-fidelity structural optimization for shock-driven fluid–structure interaction problems, in: AIAA SciTech Forum and Exposition, American Institute of Aeronautics and Astronautics, 2026.